

A Bayesian chemical evolution model of the DustPedia Galaxy M74

Francesco Calura¹, Marco Palla^{2,1}, Laura Morselli³, Emanuele Spitoni^{4,5}, Viviana Casasola⁶, Kuldeep Verma⁷, Andrea Enia¹, Massimo Meneghetti¹, Simone Bianchi⁸, Francesca Pozzi⁹, Carlotta Gruppioni¹

¹INAF – Osservatorio Astronomico di Bologna, Via Gobetti 93/3, 40129 Bologna, Italy

²Sterrenkundig Observatorium, Ghent University, Krijgslaan 281 - S9, 9000 Gent, Belgium

³CINECA National Supercomputing Center, Casalecchio di Reno, Bologna, Italy

⁴INAF - Osservatorio Astronomico di Trieste, Via Tiepolo 11, 10134 Trieste, Italy

⁵Université Côte d'Azur, Observatoire de la Côte d'Azur, CNRS, Laboratoire Lagrange, France

⁶INAF – Istituto di Radioastronomia, Via P. Gobetti 101, 40129, Bologna, Italy

⁷Department of Physics, Indian Institute of Technology (BHU), Varanasi-221005, India

⁸INAF–Osservatorio Astrofisico di Arcetri, Largo E. Fermi 5, 50125, Firenze, Italy

⁹Dipartimento di Fisica e Astronomia, Università of Bologna, via Gobetti 93/2, 40129, Bologna, Italy

11 May 2023

ABSTRACT

We introduce a new, multi-zone chemical evolution model of the DustPedia galaxy M74, calibrated by means of MCMC methods.

We take into account the observed stellar and gas density profiles and use Bayesian analysis to constrain two fundamental parameters characterising the gas accretion and star formation timescale, i.e. the infall timescale τ and the SF efficiency ν , respectively, as a function of galactocentric radius R . Our analysis supports an infall timescale increasing with R and a star formation efficiency decreasing with R , thus supporting an 'Inside-Out' formation for M74. For both τ and ν , we find a weaker radial dependence than in the Milky Way.

We also investigate the dust content of M74, comparing the observed dust density profile with the results of our chemical evolution models. Various prescriptions have been considered for two key parameters, i.e. the typical dust accretion timescale τ_0 and the mass of gas cleared out of dust by a supernova remnant, M_{clear} , regulating the dust growth and destruction rate, respectively. Two models with a different current balance between destruction and accretion i.e. with an equilibrium and a dominion of accretion over destruction, can equally reproduce the observed dust profile of M74. This outlines the degeneracy between these parameters in shaping the interstellar dust content in galaxies. Our methods will be extended to more DustPedia galaxies to shed more light on the relative roles of dust production and destruction.

Key words: galaxies: individual (NGC 0628)– galaxies: star formation - ISM: dust

1 INTRODUCTION

In the last few decades, infrared observations at low and high redshift opened our view to a complete characterisation of the coldest components of galaxies. Major results were possible thanks to Spitzer (Werner et al. 2004) and Herschel (Pilbratt et al. 2010) space telescopes, fundamental far-infrared probes that allowed the characterisation and understanding of the obscured star formation in local and distant galaxies (e. g., Rodighiero et al. 2010; Gruppioni et al. 2013). Moreover, thanks to the Atacama Large Millimetre/submillimetre Array (ALMA), we now know that at high redshift, galaxies had higher molecular gas fractions than local ones (e.g. Tacconi et al. 2010; Berta et al. 2013). These results opened a new view to the critical importance of detailed studies of the cold interstellar medium (ISM), both in the form of neutral and molecular gas. In addition to being richer in cold gas and therefore most actively star-forming, we now know also that galaxies at the peak of star formation were significantly dustier than at the present time. Infrared (IR) probes

enabled the accounting of the majority of star formation in the Universe, emphasising the fundamental role played by interstellar dust in galaxy evolution. Beside containing fundamental information on the evolutionary path of galaxies, the presence of cosmic dust affects a multitude of astrophysical processes, as it is one main contributor of the opacity of the gas, crucial for the formation of stars in molecular clouds. Moreover, dust grains represent efficient catalyst for the formation of molecular hydrogen, as their surfaces are the ideal environment for such process to occur (Gould & Salpeter 1963; Perets et al. 2005; Gavilan et al. 2014). Nonetheless, dust influences the spectral properties of galaxies across an extremely vast range of wavelengths. The most important effect of dust grains consists in the re-processing of electromagnetic radiation. This process consists in the absorption of ultraviolet and optical light, thus making dust the main physical responsible for interstellar extinction, and in its thermal re-emission in the infrared band.

For a galaxy with average properties like the Milky Way, it has been estimated that up to a half of the radiation emitted by its stars

is re-processed by interstellar dust (Popescu & Tuffs 2002; Davies et al. 2017). Since the short-wavelength light is mostly contributed by young massive stars, the IR emission of dust is regarded as one major tracer of star formation, in particular in regions where the UV emission is obscured.

Interstellar dust is also an important repository of metals, as it can incorporate heavy elements with particular properties into the solid phase, subtracting them from the interstellar gas phase, in a mechanism called dust depletion. These elements, called refractory, include abundant chemical species such as Fe, Si, Ca, Mg and C. Most of our knowledge of the nature of dust grains comes from Galactic observations and from nearby galaxies, where accurate measurements of the IR luminosity can be performed and in which the spatial distribution of dust can be explored in great detail. The local Universe offers a great variety of morphologically complex, chemically evolved galaxies where key properties such as stellar, dust and gas masses, chemical abundances, star formation rates can be measured.

A recent observational program aimed at the comprehensive study of the cold gas and dust content of local galaxies is represented by the DustPedia¹ project (Davies et al. 2017; Clark et al. 2018; De Vis et al. 2019; Nersesian et al. 2019; Casasola et al. 2020). DustPedia includes all nearby galaxies that have been observed with the Herschel Space Observatory and for which multiwavelength observations are available, in a spectral range that extends from the UV to the far-IR. The DustPedia sample probes a range of fundamental intrinsic -such as gas, stellar and dust fractions - and environmental properties, as it contains galaxies that reside in the field and in clusters (Davies et al. 2019).

One major innovative result possible thanks to the richness of this sample concerns the detailed study of spatially-resolved scaling relations, such as the galactic Main Sequence (between SFR and M_* , e. g., Elbaz et al. 2007; Noeske et al. 2007, Popesso et al. 2019a, Popesso et al. 2019b) and the Schmidt-Kennicutt relation (Schmidt 1959; Kennicutt 1998), between SFR and molecular gas surface densities, presented in Morselli et al. (2020), Enia et al. (2020) and Casasola et al. (2022).

Such broad range of available properties has enabled a series of theoretical studies aimed at using various approaches to create realistic galaxy evolution models, including numerical simulations. Dust has been rarely modelled in simulations, due mostly to the large number of parameters involved in its production and its uncertainty. Despite the significant progress experienced by these models in the last few years (McKinnon et al. 2017; Aoyama et al. 2018; Gjergo et al. 2018; Hou et al. 2019; Granato et al. 2021), their high computational cost renders the study of the parameter space of dust production and destruction problematic. The post-process modelling of some properties, like galactic spectra, is a valuable alternative, like in the recent comparison of the spectral energy distributions and physical properties of simulated and observed galaxies of Trčka et al. (2020). One problem with the post-processing approach is that it does not allow a self-consistent modelling of the main properties of interstellar dust, such as the evolution of its mass and composition, that by construction cannot be derived directly from the star formation and chemical evolution history of the simulated galaxies. Cosmological semi-analytic models for galaxy formation are a viable alternative to hydrodynamical simulations (Baugh 2006). Some of them include dust production (Valiante et al. 2011; Popping et al. 2017; Vijayan et al. 2019; Triani et al. 2020; Dayal et al. 2022) and they allow a quicker exploration of the parameter space than hy-

drodynamic simulations, still within a cosmological context. A less computationally expensive approach to theoretical galaxy evolution is represented by chemical evolution models (Tinsley 1980; Pagel 1997; Matteucci 2021). Even if in a non-cosmological context, these tools allow one to trace the evolution of the abundances of a set of chemical elements in a parametric fashion, in that the star formation and gas accretion history are not modelled directly but parametrised via a set of semi-analytic recipes. From the computational point of view these models are very light and fast to run, therefore they allow a rapid and detailed investigation of the parameter space. The results of chemical evolution models have been found to be in good agreement with the ones of cosmological models, in particular regarding the abundance pattern of stars in the Milky Way (Colavitti et al. 2008; Calura & Menci 2009; Spitoni et al. 2019). Efficient developments related to the use of such models have been possible thanks to their match with methods for Bayesian analysis. Such methods are nowadays used in several areas of astrophysics, including cosmology (Dunkley et al. 2005), studies of the propagation of cosmic rays (Putze et al. 2010), and of local active galactic nuclei (Reynolds et al. 2012), Milky Way (MW) dwarf satellites (Ural et al. 2015), semi-analytical models of galaxy formation (Kampakoglou et al. 2008; Henriques et al. 2009) and galactic chemical evolution models (e. g., Côté et al. 2016; Spitoni et al. 2020; De Looze et al. 2020). The current applications have been carried on to study mainly the MW, as it represents the best studied galaxy from the point of view of the properties of the stellar population and chemical abundances in their main components. In this paper, we are interested in the modelling of the spatial distribution of interstellar dust on galactic scales, for which an external, nearby galaxy is more suited than the MW. The DustPedia galaxy M74 (NGC 0628) is an optimal target for our study, since it is observed nearly face-on, hence it permits a very detailed mapping of a few fundamental features, such as the gas, stellar and dust density profiles (Casasola et al. 2017). In this paper, we use a Bayesian approach to build a multi-zone chemical evolution model tailored to M74. Specifically, our aim is to study the spatial distribution and internal variations of the the gas, stellar and dust components of this system.

This paper is structured as follows. In Sect. 2, we present the main observational properties of the target galaxy. In Sect 3, we present the basic ingredients of the chemical evolution model used in this study and our Bayesian fitting procedure. In Section 4, we present our results and a discussion of them, whereas in Sect. 5, we present our conclusions.

2 THE GALAXY NGC 628 (A. K. A. M74)

The data used in this work have been presented in Morselli et al. (2020) (M20) and Enia et al. (2020) (E20) and are based on multiwavelength observations of five nearby face-on spiral galaxies belonging to the DustPedia sample. DustPedia is a catalogue of 875 local systems, built originally with the purpose of studying the properties of dust in nearby galaxies of various morphological types. DustPedia includes every galaxy observed with the Herschel instrument within ~ 30 Mpc distance from the Milky Way and with a diameter > 1 arcmin. In E20, a coherent sample of galaxies with a ‘grand-design spiral’ structure was presented, characterised by Hubble stage index T between 2 and 8 (de Vaucouleurs et al. 1991; Corwin et al. 1994) and a diameter > 6 arcmin. NGC 628 (also known as M74) is observed nearly face-on (the inclination is 19.8°) and at a distance of 10.14 Mpc (E20). This galaxy has a uniform wavelength coverage, distributed across more than 20 observational bands and

¹ <http://dustpedia.astro.noa.gr/>

optimal for estimating the physical parameters analysed in this paper, i.e. the stellar, gas and dust surface densities.

E20 presented a set of multi-wavelength images of M74, ranging from the far-ultraviolet and obtained with the GALaxy Evolution eXplorer (GALEX; [Morrissey et al. 2007](#)) to the far-infrared (FIR), i.e. at $250\ \mu\text{m}$ and obtained with the Herschel Space Observatory ([Pilbratt et al. 2010](#)), showing a clear, regular spiral pattern, appreciable across 4 orders of magnitudes in wavelength (see their Fig. 1). The physical properties of M74 were determined by performing a pixel-by-pixel SED fitting, on scales between 0.39 kpc and 1.5 kpc. A grid of square cells of $8\ \text{arcsec} \times 8\ \text{arcsec}$ was constructed and, in each cell and at each wavelength, a measure of the flux was derived. A second separation in cells of fixed physical size ($1.5 \times 1.5\ \text{kpc}$) was also performed for further check of the SED fitting quality and to validate the method (for further details, see E20 and M20). The flux in every available photometric band from UV to far-IR was then obtained, along with the relative errors and the associated astrometric positions of the cell centres. In the SED fitting procedure, only cells with no more than five undetected bands were included. The discarded cells are mostly located in the outermost parts of galaxies. SED fitting was performed with the publicly available code MAGPHYS ([da Cunha et al. 2008](#)), optimal for panchromatic SED modelling of local galaxies (e.g. [Viaene et al. 2014](#)) and of resolved, sub-galactic regions ([Smith & Hayward 2018](#)). MAGPHYS allows to simultaneously model the emission observed in the UV-to-FIR regime by assuming that the whole energy output is balanced between the radiation emitted at UV/optical/near-infrared wavelengths and the amount absorbed by dust and then re-emitted in the FIR. The physical scales probed in this work (0.39 kpc) are such that the energy-balance criterion holds (E20 and references therein). In the energy-balance criterion between stellar and dust emission, the UV-optical photons emitted by young stars are absorbed (and scattered) by dust grains in star-forming regions and more diffuse parts of the ISM, and the heated dust then reradiates the absorbed energy in the IR (e.g., [Miettinen et al. 2017](#); [Bianchi et al. 2018](#)). The energy-balance criterion holds on scales in which the visible stellar component is co-spatial with the obscured, dust-emitting component of a star-forming region. This physical scale, typically of $200\text{--}400\ \text{pc}$ (E20; M20) happens to be of the same order or above the region size where a ‘molecular star formation law’ can be observationally retrieved, i.e. where the scaling between the averaged molecular gas surface density and the star formation rate is $\Sigma_{\text{SFR}} \propto (\Sigma_{\text{H}_2})^N$, with $N \sim 0.5\text{--}1.5$ (e.g., [Bigiel et al. 2008](#); [Schruba et al. 2010](#); [Casasola et al. 2015](#)), i.e. where the Schmidt-Kennicutt law holds ([Khoperskov & Vasiliev 2017](#)). The pixel size of M74 is at the upper edge of this condition, but still suitable for these purposes.

By means of a Bayesian approach, the code determines the posterior distribution functions of various physical parameters by fitting the observed photometric data to the modelled emission. The latter is calculated from a set of native libraries composed of 5×10^4 stellar population spectra, with varying star formation histories and derived from the [Bruzual & Charlot \(2003\)](#) spectral library. Such library allows for a uniform exploration of a few fundamental parameters, such as stellar age, star formation timescale and metallicity. The stellar emission libraries are associated to 5×10^4 two-component SEDs ([Charlot & Fall 2000](#); [da Cunha et al. 2008](#)), which take into account the emission from stellar birth clouds and the diffuse interstellar medium. SED fitting on the integrated photometry of the DustPedia data was also performed (E20), as a further validation of the analysis and to derive large-scale properties of the galaxy, such as total SFR and the gas mass. The stellar and dust mass values obtained in each cell were directly taken from the MAGPHYS outputs. MAGPHYS

models the dust emission as the sum of two components, the one coming from stellar birth clouds (e.g. PAH, mid-IR continuum and grains in thermal equilibrium) and a colder one from the ambient ISM ([da Cunha et al. 2008](#)).

As for the gas mass, in each cell we consider that it is given by the sum of the neutral and molecular gas mass, including also the Helium contribution. The neutral hydrogen mass surface densities have been obtained from the 21 cm maps in the framework of the THINGS survey (The HI Nearby Galaxy Survey; [Walter et al. 2008](#)) performed with the Very Large Array (VLA), with a 6 arcsec and 10 arcsec resolution in the robust and natural weighting, respectively. The neutral gas surface density has been estimated from equation 5 of [Walter et al. \(2008\)](#). The molecular gas surface density has been computed by means of $^{12}\text{CO}(2\text{--}1)$ intensity maps obtained in the HERACLES survey (The HERA CO-Line Extragalactic Survey; [Leroy et al. 2009](#)), performed with IRAM 30 with an angular resolution of 11 arcsec.

We defer to M20 for further details on the methods used for estimating the neutral and molecular gas mass in M74. Fig. 1 shows a dust mass map (left) and estimates of the stellar, gas and dust surface density profiles (right) of M74.

3 MODEL DESCRIPTION

The chemical evolution model used in this paper was originally developed to study the abundance pattern of the Milky Way (e.g., [Matteucci & Francois 1989](#); [Grisoni et al. 2018](#); [Palla et al. 2020b](#)). We implicitly assume that the baryonic mass of any spiral galaxy is dominated by a thin disc of stars and gas, in analogy with the Milky Way. The disc is composed of several independent rings, each 1 kpc-wide, without exchange of matter between them.

In chemical evolution models, the time-evolution of the fractional mass of the element i in the gas within a galaxy and at the galactocentric radius R , $G_i(R, t)$ is described by the following equation (here in compact form, for the extended form see, e.g., [Matteucci 2012](#)):

$$\dot{G}_i(R, t) = -\psi(R, t)X_i(R, t) + \mathcal{R}_i(R, t) + \dot{G}_{i,\text{inf}}(R, t). \quad (1)$$

In Eq. 1, $G_i(R, t) = X_i(R, t)G(R, t)$, where $X_i(R, t)$ represents the abundance (in mass) of the element i (for which, the sum over all elements in the gas is equal to unity) and $G(R, t)$ is the total gas fraction. The quantity $\psi(R, t)$ is the star formation rate (SFR), namely the amount of gas turning into stars per unit time. This quantity is expressed by the Schmidt-Kennicutt relation ([Schmidt 1959](#); [Kennicutt 1998](#)) law:

$$\psi(R, t) = \nu \Sigma_{\text{gas}}(R, t)^K, \quad (2)$$

where $K = 1.5$, Σ_{gas} is the gas surface density and ν is the star formation efficiency (in Gyr^{-1}), assumed to be a function of the radius R and parametrised as described later in Sect. 3.1. The motivation for assuming a radius-dependent SF efficiency is that, as shown in a few previous studies, it is not possible to reproduce some specific observables of the MW, such as the abundance gradients observed in the disc, by assuming a constant SF efficiency ([Colavitti et al. 2009](#); [Grisoni et al. 2018](#); [Palla et al. 2020b](#)).

The quantity $\mathcal{R}_i(R, t)$ is the returned fraction of matter in the form of an element i restored by stars into the ISM through stellar winds, Type Ia and Type II supernova (SN) explosions and computed from the nucleosynthesis prescriptions. In this work, we assume for low-intermediate mass stars (LIMS, i.e. stars with initial mass $m < 8M_{\odot}$) the stellar yields calculated by [van den Hoek & Groenewegen \(1997\)](#),

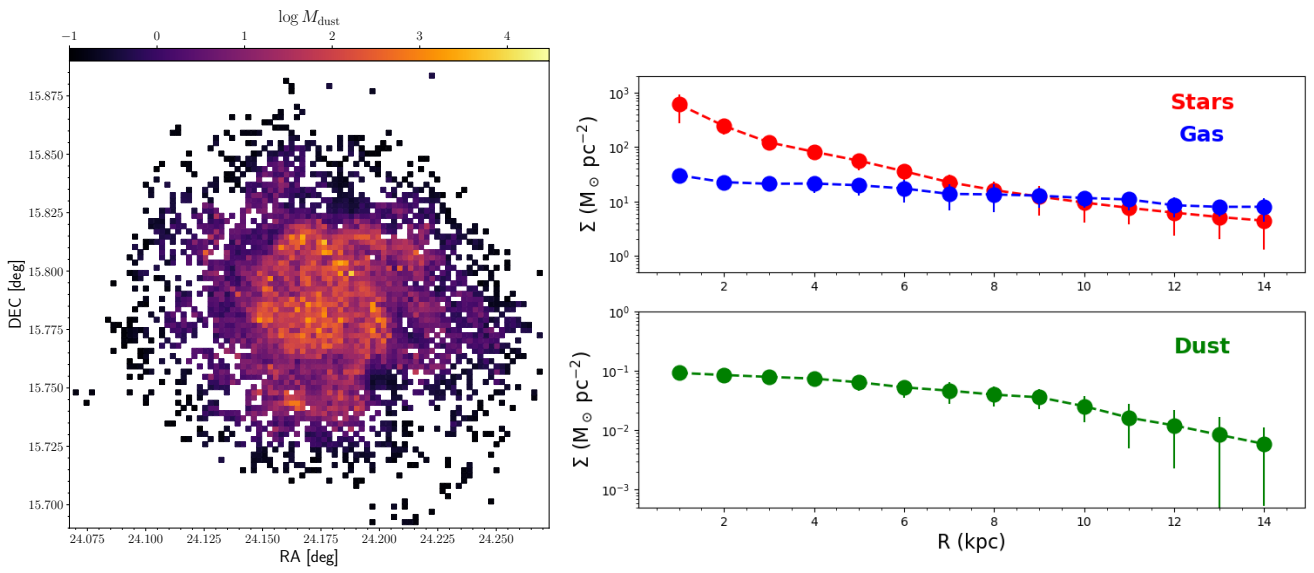


Figure 1. Left: observed dust mass map of M74. In each pixel, the dust mass was derived with the methods described in Sect. 2. Right: observed stellar and gas surface density profiles (upper panel) and dust density profile (bottom panel) of M74. The data used for the calculation of the profiles are from Morselli et al. (2020) and Enia et al. (2020).

whereas for core-collapse and Type Ia supernova (SNe) we adopt the prescriptions of François et al. (2004) and Iwamoto et al. (1999), respectively, with a Scalo (1986) stellar initial mass function (IMF). By means of our adopted set of yields it is possible to reproduce the chemical abundance pattern of the solar neighbourhood (e.g., Spitoni et al. 2019; Vincenzo et al. 2019; Palla et al. 2022).

The third term in Eq. (1) is the infall rate, expressed as:

$$\dot{G}_{i,\text{inf}}(R, t) = A(R)X_{i,\text{inf}}(R)e^{-\frac{t}{\tau(R)}}, \quad (3)$$

where $X_{i,\text{inf}}$ is the abundance of the element i in the infalling material, assumed of primordial composition. The infall timescale $\tau(R)$ is determined from the available observational constraints of M74 by means of the MCMC analysis described in Sect. 3.1. The quantity $A(R)$ is determined from the observed total surface mass density profile of M74.

In our model, we assume that spiral galaxies do not experience galactic winds. In general, galactic winds are known to play an important role in galaxy evolution and the modelling of this process is a very active field (e. g., Somerville & Davé 2015; Zhang 2018). A plethora of models have shown that when proto-galaxies are small and are characterised by shallow potential wells, strong feedback activity resulting from intense star formation can trigger massive outflows, in which the dense star-forming gas can leave the parent galaxy (Naab & Ostriker 2017 and references therein). In cosmological simulations, the generation of massive outflows is important to avoid the overproduction of stars, to remove low angular momentum-material and thus for producing realistic discs (Brook et al. 2011; Marinacci et al. 2014; Murante et al. 2015; Vogelsberger et al. 2020 and references therein).

Also observations of local discs show that they still have an important role, and that they can be described by biconical flows of multiphase gas and dust perpendicular to the galaxy (Rupke 2018).

Our assumption of neglecting the effects of winds in the long-term evolution of a massive galactic disc is supported by other models that include the evolution of the infall and outflow rates of MW-like disc galaxies, showing that the latter are generally sub-dominant with respect to the former (Toyouchi & Chiba 2015). Furthermore,

our assumption is strengthened by the fact that a large fraction of the material ejected through outflows is later reaccreted. This is supported by cosmological simulations of galactic discs of different mass, which confirm that the majority of the mass ejected by the disc in galaxies with virial mass $> 10^{11} M_{\odot}$ (encompassing the mass of M74) is reaccreted (Christensen et al. 2018, see also Oppenheimer & Davé 2008; Davé et al. 2011; Hopkins et al. 2023). Note that our non-cosmological models for galactic discs do not exclude that winds may have an important role in their low-mass progenitors at early times, as shown by the history of the Milky Way and of its building blocks (Vincenzo et al. 2019).

3.1 The best model of M74 through Bayesian analysis

The best-fit chemical evolution model of M74 has been obtained by means of a Bayesian analysis based on Markov Chain Monte Carlo (MCMC) methods. We briefly recall our main assumptions and refer the reader to Spitoni et al. (2020) for a more detailed description of the fitting method.

In the context of parameter estimation, Bayes' theorem enables the calculation of the posterior probability distribution (PPD) of the parameters, as expressed by

$$P(\Theta|\mathbf{x}) = \frac{P(\Theta)P(\mathbf{x}|\Theta)}{P(\mathbf{x})}, \quad (4)$$

where \mathbf{x} represents the set of observables, Θ the set of model parameters, $P(\mathbf{x}|\Theta) \equiv L$ the likelihood, defined as the probability of observing the data given the model parameters. In this work, the set of observables is represented by the stellar and gas surface density profiles at the present time, respectively Σ_{\star} and Σ_{gas} , computed over $N = 14$ radial bins (see the right panel of Fig. 1), i.e. $\mathbf{x} = \{\Sigma_{\star}, \Sigma_{\text{gas}}\}$.

In this study, we statistically constrain the behaviour of the gas accretion timescale and the star formation efficiency with galactocentric radius. The assumptions of radial dependent infall timescale and SF efficiency have been widely adopted in previous chemical evolution models. In the framework of the inside-out model for the formation of the Milky Way, Matteucci & Franco (1989) introduced

a radius-dependent time-scale for the exponential infall rate of the Galactic disc, increasing linearly as a function of the galactocentric radius (see also Romano et al. 2000). On the other hand, a variable SF efficiency as a function of galactocentric radius was introduced by Colavitti et al. (2009) as an additional mechanism to explain the abundance gradients in the MW disc (see also Spitoni et al. 2015; Palla et al. 2020b).

In our approach, we consider a set of 4 free parameters $\Theta = \{A, B, C, D\}$, in the following two equations:

$$\tau [\text{Gyr}] = A \cdot R + B \quad (5)$$

and

$$\nu [\text{Gyr}^{-1}] = \frac{C}{R} + D. \quad (6)$$

To define the likelihood in eq. 4, we assume that the uncertainties on the observables are normally distributed. In this case, the logarithm of the likelihood can be written as:

$$\ln L = - \sum_{n=1}^N \ln \left((2\pi)^{d/2} \prod_{j=1}^d \sigma_{n,j} \right) - \frac{1}{2} \sum_{n=1}^N \sum_{j=1}^d \left(\frac{x_{n,j} - \Sigma_{n,j}}{\sigma_{n,j}} \right)^2, \quad (7)$$

where $N = 14$ is the number of radial bins, $x_{n,j}$ and $\sigma_{n,j}$ are the measured value and associated uncertainty, respectively, of the j -th observable and in the n -th radial bin, whereas $\Sigma_{n,j}$ is the theoretical j -th mass surface density (i.e. for the gas or stars) at the present day in the n -th radial bin, with $d = 2$.

The calculation of the PPD defined in eq. 4 requires the specification of the priors on the 4 model parameters. In our sampling of the PPD, for all the parameters we consider a flat prior in the range $(-50, +50)$; only combinations that lead to positive τ and ν are admitted. The affine invariant MCMC ensemble sampler, "emcee: the mcmc hammer" code² (Goodman & Weare 2010; Foreman-Mackey et al. 2013) has been used to sample the PPD.

3.2 Dust evolution prescriptions

In this work, we adopt the same formalism used in previous works which included the chemical evolution of dust in galaxies of various morphological types (Dwek 1998; Calura et al. 2008; Gioannini et al. 2017b; Palla et al. 2020a). The equation used to determine the amount of the chemical element i contained into dust grains is:

$$\dot{G}_{i,d}(R, t) = -\psi(t)X_{i,d}(R, t) + R_{i,d}(R, t) + \frac{G_{i,d}}{\tau_{i,accr}}(R, t) - \frac{G_{i,d}}{\tau_{i,destr}}(R, t) \quad (8)$$

Similarly to Eq. (1), $G_{i,d}(R, t) = X_{i,d}(R, t)G(R, t)$, where $X_{i,d}(R, t)$ represents the abundance (in mass) of the element i present in dust grains. The first term on the right-hand side of Eq. (8) accounts for the amount of dust destroyed by astration, i.e. incorporated into new stars. $R_{i,d}(R, t)$ accounts for stellar dust production, which in our model is from asymptotic giant branch (AGB) stars and core-collapse SNe. In low and intermediate mass stars (LIMS, i.e. stars with mass $0.8 \leq M_{\odot} \leq 8$), dust is produced during the AGB phase. For AGB stars, in this work we use the metallicity-dependent dust yields of Dell'Agli et al. (2017). Stars more massive than $8M_{\odot}$ end their life as core-collapse (CC) SNe and are the main producers of dust. For these sources, we assume the dust yields of Bianchi & Schneider (2007) that, as shown in Gioannini et al. (2017a), provide

dust mass values intermediate between other prescriptions from the literature.

The third term on the right side of Eq. (8) accounts for dust accretion (or growth) in molecular clouds. In this process, occurring in the coldest and densest regions of the ISM, pre-existing seeds of dust can grow in size as due to accretion of further refractory elements on their surface (e. g., Savage & Sembach 1996; Hirashita & Kuo 2011; Inoue 2011; Asano et al. 2013; Martínez-González et al. 2021; Konstantopoulou et al. 2022), enabling a significant increase of the global dust mass (e.g. Dwek 1998; Asano et al. 2013; Mancini et al. 2015; De Vis et al. 2017). The dust accretion rate is regulated by the accretion timescale τ_{accr} . For a given element i , this quantity can be expressed as:

$$\tau_{i,accr} = \frac{\tau_0}{(1 - f_i)}, \quad (9)$$

where $f_i = G_{i,d}(t)/G_i(t)$ is the dust-to-gas ratio for the element i at the time t and τ_0 is the characteristic dust growth timescale. This formalism was first introduced by Dwek (1998), in which the key quantity τ_0 was assumed constant and generally of the same order of magnitude of the typical molecular cloud lifetime (see also Calura et al. 2008). Later, more elaborate assumptions have been proposed by other authors, with a dependency on fundamental galactic parameters such as metallicity and cold gas fraction (e. g., Asano et al. 2013).

The fourth term of Eq. (8) accounts for dust destruction, occurring in the warm and hot phases of the ISM mostly as due to exploding SNe. In this process, the refractory material incorporated in dust grains and accelerated by SN shocks is cycled back into the gas phase via various mechanisms (evaporation in grain-grain collisions, sputtering, thermal sublimation, desorption, see McKee 1989, Jones et al. 1996).

Similarly to dust accretion, dust destruction is expressed in terms of a grain destruction timescale τ_{destr} , which can be written as:

$$\tau_{i,destr} = \frac{G_i(t)}{(\epsilon M_{swept})SN_{rate}}, \quad (10)$$

where SN_{rate} is the sum of the CC and Type Ia SN rates, M_{swept} is the ISM mass swept by a SN shock and ϵ is the efficiency of grain destruction in the ISM.

The product of the two latter terms represents the ISM mass completely cleared out of dust by a SN:

$$M_{clear} = \epsilon M_{swept}. \quad (11)$$

In this paper, we will study in detail the roles of the main quantities regulating dust growth and destruction, i.e. τ_0 and M_{clear} and see how they determine the dust content of M74, as traced by the observed dust mass profile as a function of galactic radius.

The Bayesian approach requires a specific parameterization of a given process as a function of fundamental quantities that regulate them, such as the infall timescale and the SF efficiency as a function of the galactocentric radius (see Equations 5 and 6).

In this work, we want to test various prescriptions for quantities regulating both destruction and accretion, in which the dependence on some fundamental physical variables is diversified. Testing every single prescription by means of a MCMC would be very challenging from a computational point of view; therefore, in this work we choose to model the evolution of dust without a Bayesian approach. In the forthcoming future, the next step will be to adopt a Bayesian method to treat also the evolution of dust.

² <https://emcee.readthedocs.io/en/stable/>; <https://github.com/dfm/emcee>

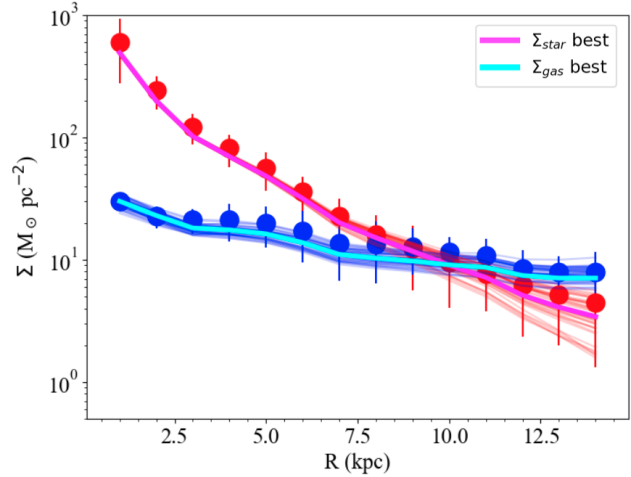
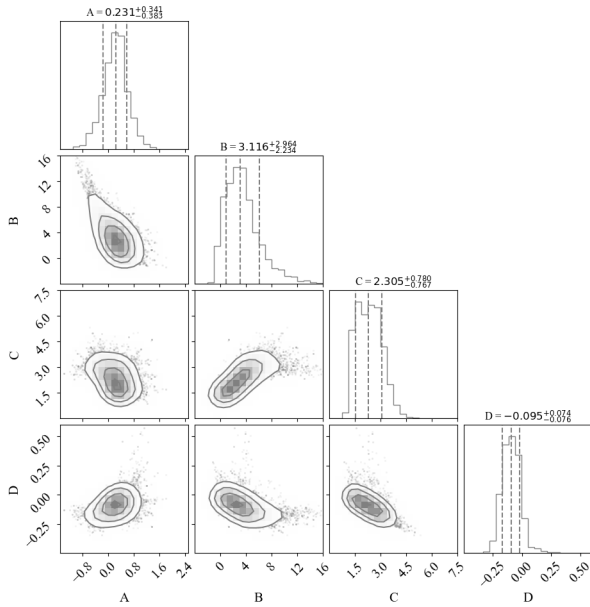


Figure 2. Left panel: posterior probability density function of the parameters used to model the accretion and SF history of M74. The best-fit value obtained for the parameter (defined in Sect. 4) is reported on the top of each column, along with the associated uncertainties. The results of the best-fit model are shown in the right panel, where the thick magenta and cyan lines represent the best-fit stellar and gas surface density as a function of radius, respectively. The blue and red thin lines represent the range of models obtained from the Monte Carlo walkers at the last step that are consistent with the observed profiles, i.e. characterised by Σ_{gas} and Σ_{star} values within the observed error bars.

4 RESULTS

In this section we present the results of the best-fit chemical evolution model of M74, obtained from the observational constraints, i.e. the observed gas and stellar density profiles of M74, and by means of the Bayesian method described in Sect. 3.1. The best model is then used to study the star formation history and the properties of the dust in our target galaxy, in order to derive constraints on a few fundamental prescriptions adopted in our model.

We have used 100 walkers to sample the parameter space. The chains have been run for 500 steps. The MCMC reaches convergence in less than 125 steps, used as a warm up phase (burn-in). Therefore, the PPD has been built using the final 375 steps. As an additional check, we also verified that the acceptance fraction of walkers is about 0.4, well within the range of values recommended (between 0.2 and 0.5).

The posterior probability density function of the parameters is shown in the left panel of Fig. 2, where the best-fit values obtained for our set of parameters are also reported with their uncertainties.

For each parameter, we compute the best-fit value, the lower and upper uncertainty from the median, the 16-th and the 84-th percentile of the distribution (reported on the top of each column of Fig. 2), respectively.

We show the results of the best-fit model in the right panel of Fig. 2 (thick magenta and cyan lines), compared to the observed profiles. The thin lines in Fig. 2 represent the range of models within the 16th and 84th percentiles, hence corresponding approximately to $1 - \sigma$ error bars of the best-fit models.

4.1 Star formation and infall timescale as a function of radius

Fig. 3 shows the infall timescale τ (green solid line) and the SF efficiency ν (red solid line) as a function of galactocentric radius R of the best model obtained for M74 through our Bayesian analysis.

As for the best-fit $\tau - R$ function (green line), an analogue relation was found for our Galaxy by Romano et al. (2000), expressed by

$$\tau_{D,MW} = 1.03 R - 1.267 \text{ Gyr} \quad (12)$$

and describing the 'Inside-Out' formation model of the disc component of the MW.

The relation in Eq. 12 is able to account for various constraints, i.e. the 'G-dwarf' metallicity distribution observed in the solar neighbourhood and in other regions of the Galactic disc, the gas density profile and the Galactic abundance gradients (see also Chiappini et al. 2001).

Also for M74, our analysis supports an inside-out formation scenario, but the flatter shape of the $\tau - R$ function obtained here suggests more similar gas accretion rates at different radii with respect to the MW. For comparison, the accretion timescales of M74 at 2 kpc and 14 kpc are ~ 3.8 Gyr and ~ 6 Gyr, respectively, whereas in the Milky Way, at the same radii Romano et al. (2000) derived accretion timescales of 1 Gyr and 13 Gyr, respectively.

In principle, beside a smaller average stellar age, a flatter accretion timescale with radius is expected to produce a lower dispersion of stellar age than in the Milky Way. It is however worth stressing that the single-infall model used here differs by construction from the one used for our Galaxy, which allows for a better characterisation of the various sub-components, for which much more observational constraints are available. In particular, valuable constraints in this context are represented by the stellar chemical abundance pattern, at the moment available for our Galaxy and for a few of its satellites only, which provide an insightful picture of the past evolution of such systems and therefore allows one to have tighter constraints for their accretion history.

The red line in Fig. 3 shows the SF efficiency $\nu(R)$ of M74 derived in this work. Also in this case, it is interesting to compare this quantity to the analog relation found in the MW. Palla et al. (2020b) used the two-infall model to constrain some fundamental properties of

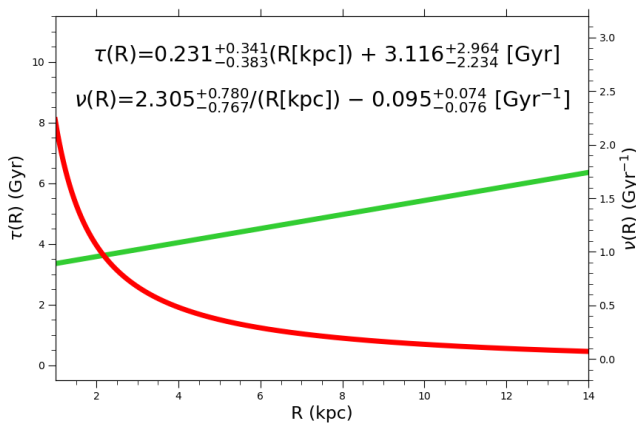


Figure 3. Accretion timescale τ (green solid line and left-side y-axis) and SF efficiency ν (red solid line and y-axis on the right) as a function of galactocentric radius R of the best model obtained for M74 through our Bayesian analysis.

the thin and thick Galactic discs, including the SFR profile and the abundance gradients, considering different chemical elements (including Mg, Fe, N, O). Again, their model is more complex than ours since, besides including two separate infall events for different sub-components, they also take into account radial gas flows. A variable efficiency of star formation is considered for the thin disc and the effects of other parameters are investigated, including the delay between the formation of the two discs. They find that the assumption of a variable SF efficiency along the disc plays a fundamental role in reproducing the observed abundance gradients (see also Grisoni et al. 2018). Although the trend is similar, i.e. characterised by decreasing ν at increasing radii, the $\nu - R$ relation derived here, which spans a range between $\sim 2 \text{ Gyr}^{-1}$ in the innermost regions and $\sim 0.1 \text{ Gyr}^{-1}$ in the outskirts, is less extreme than the one found in the MW, which ranges between $\sim 5 \text{ Gyr}^{-1}$ and $\sim 0.1 \text{ Gyr}^{-1}$.

As additional check, we have compared the metallicity gradient obtained with the best model of M74 to a set of available observations.

The used metallicity tracer is oxygen. We show in Fig. 4 the data from the DustPedia compilation of De Vis et al. (2019), obtained using two different metallicity calibrators: the simplest N2 calibrator, which is based on the ratio between [NII] $\lambda 6584$ and the adjacent H α line (thus depending little on dust extinction), and the O3N2 method, that uses [OIII] $\lambda 5007$, [NII] $\lambda 6584$, H β and H α lines (Pettini & Pagel 2004). It is well known that, when using different diagnostics, the metallicity measures are significantly sensitive to the adopted calibration (Kewley & Ellison 2008; Calura et al. 2009; Maiolino & Mannucci 2019). The difference between the two profiles is useful to envisage the uncertainties in the calibration schemes. As shown in Fig. 4, our model can satisfactorily account for the observed metallicity gradient, in particular the one measured from the O3N2 line ratio, across the entire radial range of the observations (from $R=1 \text{ kpc}$ to $R \sim 14 \text{ kpc}$). As for the gradient measured from N2, in the innermost regions ($R < 5 \text{ kpc}$) the data indicate a flatter gradient than what found in our best model. Investigating the reason of the discrepancy between the N2 measures and the model results is beyond the scope of the present work.

In Fig. 5 we show the evolution of the gas mass, stellar mass and star formation history of the best model, obtained as described in this

section. We also show the evolution of the dust mass of the two best models described in Sect. 4.3.1 and 4.3.2.

In Table 1, we present a few observational features of M74 and compare them to the results of our best models. The observed and theoretical gas, stellar and dust masses have been computed integrating the respective profiles. M74 has an observed dust mass of $2 \times 10^7 M_{\odot}$, similar to the of other spiral galaxies of similar stellar mass (Pastrav 2020). The results of the comparison between the measured dust mass and the models will be discussed in the Sect. 4.3.

4.2 Effects of radial flows

Radial gas flows may take place as a dynamical consequence of infall (Spitoni & Matteucci 2011; Bilitewski & Schönrich 2012). The cosmological accretion of gas is expected to occur mostly in the outskirts of galactic discs (Ho et al. 2019). The infalling gas has a lower angular momentum than the gas orbiting within the disc, and the mixing between the two is expected to induce a net, inward-directed radial flow (Mayor & Vigroux 1981), with a velocity in the range of a few km s^{-1} (Lacey & Fall 1985). Radial flows may also originate as a consequence of the viscosity of the gas (Thon & Meusinger 1998) and of spiral density waves that may lead to large-scale shocks and energy dissipation (Spitoni & Matteucci 2011 and references therein).

In our reference multi-zone model we have neglected radial flows, i.e. we have assumed that no exchange of matter can occur between two adjacent rings. This assumption relies upon the results of various studies, who have shown that, under reasonable conditions, radial flows alone have a marginal role in reproducing the abundance gradients measured in the MW disc (Portinari & Chiosi 2000; Spitoni & Matteucci 2011; Palla et al. 2020b), and that the latter are the result of the interplay of various processes, including a star formation threshold, an efficiency of star formation and infall law varying with radius (Colavitti et al. 2009; Palla et al. 2020b).

The study of radial gas flows in local spiral galaxies is a recent, growing field (Di Teodoro & Peek 2021) but their effects on the properties of other galaxies have rarely been addressed. In this Section, we include radial gas flows in the model of M74 and show their effects on the observables considered in this work, i.e. the stellar and gas density profiles and the metallicity gradient.

The model used here is described in Spitoni & Matteucci (2011), Mott et al. (2013), Palla et al. (2020b) and is based on the formalism of Portinari & Chiosi (2000). It is convenient to define the k -th shell of the galactic disc in terms of the galactocentric radius R_k , whose inner and outer edges are $R_{k-1/2}$ and $R_{k+1/2}$, respectively. Through these edges, gas inflow can occur with velocity $v_{k-1/2}$ and $v_{k+1/2}$, respectively, with velocities assumed to be positive outward and negative inward.

The net radial flow rate at galactocentric radius R_k and time t is included as a further additive term in Eq. 1 and is expressed as:

$$\dot{G}_{i,\text{rf}}(R_k, t) = -\beta_k G_i(R_k, t) + \gamma_k G_i(R_{k+1}, t), \quad (13)$$

where β_k and γ_k are, respectively:

$$\beta_k = -\frac{2}{R_k + \frac{R_{k-1} + R_{k+1}}{2}} \times \left[v_{k-1/2} \frac{R_{k-1} + R_k}{R_{k+1} - R_{k-1}} \right] \quad (14)$$

$$\gamma_k = -\frac{2}{R_k + \frac{R_{k-1} + R_{k+1}}{2}} \times \left[v_{k+1/2} \frac{R_k + R_{k+1}}{R_{k+1} - R_{k-1}} \right] \frac{\Sigma_{(k+1),\text{T}}}{\Sigma_{k,\text{T}}}. \quad (15)$$

Table 1. Summary of the main observational properties of M74 and as computed by means of our best models.

	D (Mpc)	D ₂₅ ($''$)	Hubble type	M _{gas} (M _⊙)	M _* (M _⊙)	SFR (M _⊙ yr ⁻¹)	M _{dust} (M _⊙)
M74 (observed)	9.0 ¹	10.0 ²	Sc ³	8.5×10^9	2.0×10^{10}	0.7 ⁴	2.0×10^7
Model (5 ¹)	-	-		7.0×10^9	1.68×10^{10}	0.9	1.96×10^7
Model (9 ¹)	-	-		7.0×10^9	1.68×10^{10}	0.9	2.26×10^7

1: Casasola et al. (2017)

2: D₂₅ is defined as the length corresponding to the projected major axis of a galaxy at the isophotal level of 25 mag arcsec⁻² in the B-band (Casasola et al. 2017). At the distance of M74, this corresponds to a diameter of 26.18 kpc.

3: From the NED database.

4: Gusev et al. (2014)

$\Sigma_{(k+1),T}$ and $\Sigma_{k,T}$ are the total present-day density profiles at the radius R_{k+1} and R_k , respectively.

In this parametrization the most critical quantity is the radial velocity pattern, expressed by v_k . We have studied the effects of an inward-directed radial gas flow, testing various values for v_k and various assumptions for the radial dependence of the infall and SF law.

As for the velocity pattern, we have considered both constant and radial-dependent values, previously considered to model radial flows in the Milky Way (Grisoni et al. 2018; Palla et al. 2020b). As for the infall timescale and star formation efficiency radial dependence, beside the ones of best-fit model described in Sect. 4.1, we have tested other assumptions, including constant τ and ν (i.e. no radial dependence) and other, intermediate choices between constant and the ones of the best-fit model.

As for the best-fit model obtained through Bayesian analysis with added radial flows, none of the tested assumptions for the velocity pattern could reproduce the considered constraints simultaneously. The results of one of these cases is shown in the left panels of Fig. 6, where constant radial velocity $v_k = -0.5$ km s⁻¹ was assumed. This is a low value in the framework of models generally suited to account for the velocity pattern of the MW disc (e. g., Palla et al. 2020b). Although it does not have any major effect on the present-day gas and stellar mass profiles but a slight steepening, such a low value is enough to steepen significantly the metallicity gradient, as shown in the bottom-left panel of 6. We have verified that other velocity patterns assumed for the MW disc, including a higher (in modulus) constant velocity $v_k = -1$ km s⁻¹ and a variable velocity $v_k = -(\frac{R_k}{4} - 1)$ km s⁻¹ (Grisoni et al. 2018) cause a steepening also of the density profiles and do not improve the fit to the observed metallicity gradient.

In the right panels of 6, we show the results of a couple of models with different assumptions regarding the radial dependence of τ and ν . One model ('Constant $\tau(R)$ and $\nu(R)$ ', solid lines), is with constant $\tau = 4$ Gyr and $\nu=0.45$ Gyr⁻¹ at all radii. These values for τ and ν are similar to the ones of the best model obtained with the MCMC at 4 kpc.

Another model ('Intermediate $\tau(R)$ and $\nu(R)$ ', dashed lines in the right panels of Fig. 6) is characterised by values for the quantities A and C defined in Sect. 3.1 that are approximately half of the best-fit model, but values for $\tau(R)$ and $\nu(R)$ at $R = 4$ kpc that are comparable to the ones of this model. These choices are certainly arbitrary; however, more tests have been performed by anchoring the relations to the τ and ν of the best-fit model at other values of R , without any improvement in the results.

Our results are useful to illustrate the overall effects of an inward-directed velocity pattern. These models provide a stellar profile in

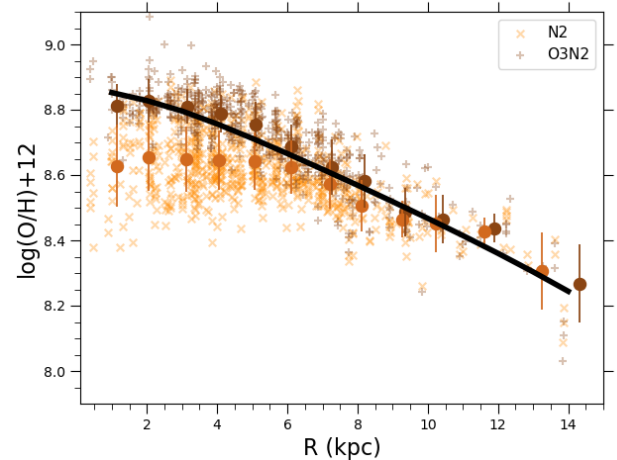


Figure 4. Metallicity gradient of the best model of M74 (black solid line) compared to a set of available observations. The metallicity tracer is oxygen, for which two strong line calibrations (the N2 [orange crosses] and the O3N2 [brown crosses]) have been used to derive the abundances as a function of radius (see De Vis et al. 2019, Bianchi et al. 2022). The brown and orange circles represent the average abundances computed at different radial bins and considering both sets of abundances. In each radial bin, the brown vertical bar associated to the computed average abundance represents the $1 - \sigma$ uncertainty.

agreement with data and within the error bars at almost all radii, an acceptable fit to metallicity gradient but a gas density profile steeper than the available observations. As shown in Fig. 5, the overall effects on the star formation history are modest.

Although our results can certainly be improved with a more thorough investigation of the parameter space, the analysis carried out in this Section highlights that, by assuming significant net radial inflows in the galaxy, we are not able to reproduce the different observational constraints of M74, i.e. the stellar density, gas density and metallicity gradient simultaneously. The same conclusion also holds by varying the prescriptions for the radial dependence of gas accretion and SF law.

At present and based on extant data, it is not possible to firmly assess the radial velocity pattern of the gas in local galaxies. A systematic study of gas flows in local spirals based on atomic hydrogen emission line high-sensitivity data indicates that the magnitude of radial inflow motion seems small, of the order of a few 0.1 M_⊙/yr and a factor 5-10 smaller than the typical SFR values (Di Teodoro & Peek 2021). This suggests that radial inflows alone are not strong enough to sustain star formation in local spiral galaxies.

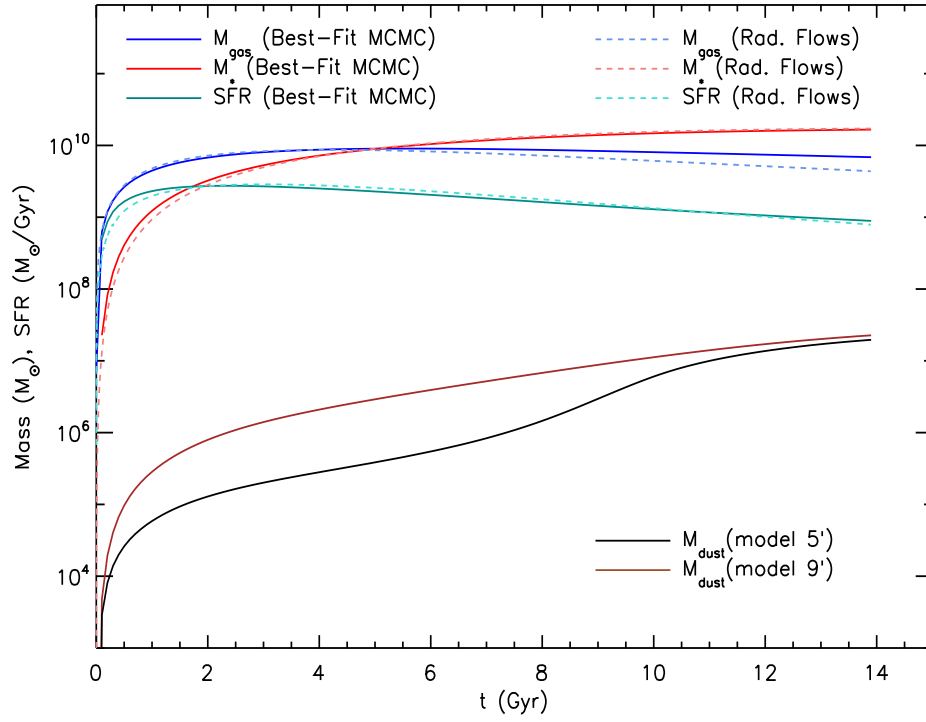


Figure 5. Evolution of the gas mass (blue solid line), stellar mass (red solid line) and star formation history (dark-cyan solid line) of the best-fit model obtained with our bayesian analysis described in Sect. 3.1. The light-blue, coral and turquoise dashed lines are the evolution of the gas mass, stellar mass and star formation history, respectively, of the ‘Intermediate $\tau(R)$ and $\nu(R)$ ’ model, which includes radial flows and is described in Sect. 4.2. The black and brown solid lines are the dust mass of the models 5’ and 9’ described in Sect. 4.3.1 and 4.3.2, respectively.

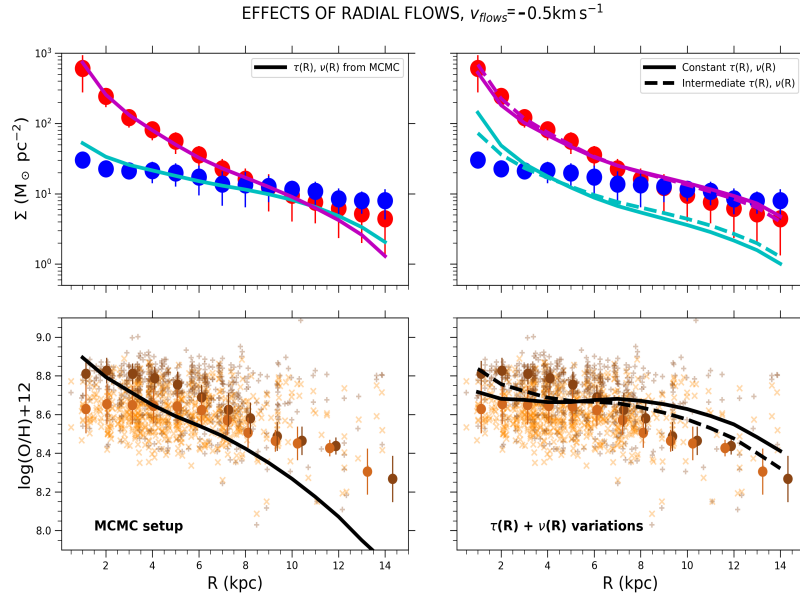


Figure 6. Top-left panel: stellar (solid magenta line) and gas (solid dark cyan line) surface density as a function of radius of the best-fit model for M74 obtained with the bayesian analysis plus radial flows, described in Sect. 4.2. The blue and red solid circles are as in Fig. 1. Bottom-left panel: metallicity gradient of the best-fit bayesian model of M74 plus radial flows (black solid line) compared to a set of observations (other symbols as in Fig. 4). Top-right panel: stellar (magenta lines) and gas (dark cyan lines) surface density profiles of the model with constant $\tau(R)$ and $\nu(R)$ (solid lines) and intermediate $\tau(R)$ and $\nu(R)$ (dashed lines), both including radial flows and described in Sect. 4.2. The blue and red solid circles are as in Fig. 1. Bottom-right panel: metallicity gradient of the model with constant $\tau(R)$ and $\nu(R)$ (solid line) and intermediate $\tau(R)$ and $\nu(R)$ (dashed line). Other symbols are as in Fig. 4.

4.3 Dust density profile

Understanding the roles of destruction and accretion in regulating the dust mass budget in galaxies represents one major challenge in galaxy evolution studies. How these mechanisms depend on key galactic properties, such as radius and SFR, is not known, and various authors have proposed different prescriptions to include their effects in galactic evolution models.

In the following, we exploit the best model obtained for M74 to test various prescriptions for these two processes and compare our results with one key observational constraint available for this galaxy, i.e. the dust surface density profile.

In particular, we test different formalisms for the parameter regulating the accretion timescale τ_0 of Eq. 9 and for the destruction timescale, expressed by the 'cleared mass' parameter M_{clear} of Eq. 10. A summary of the models considered in this work and adopting different prescriptions for accretion and destruction is presented in Table 2.

4.3.1 Asano et al. (2013) prescriptions for dust accretion

Asano et al. (2013) investigated the role of dust mass growth in the ISM by means of a closed-box chemical evolution model which included stardust production, destruction by SN shocks and accretion. They emphasised the role of the interstellar metallicity in determining the dust accretion timescale, identifying a critical metallicity value, decreasing with decreasing SF efficiency, above which accretion becomes the primary process in regulating the galactic dust budget, also causing the strong depletion of heavy elements from the gas phase.

In the model of Asano et al. (2013), the dust accretion timescale τ_0 of Eq. 9 is expressed as:

$$\tau_0 = \frac{\tau_g}{X_{\text{cold}}} \quad (16)$$

where τ_g is the characteristic dust growth timescale within a molecular cloud and X_{cold} is the mass fraction of dense cold clouds in a galaxy. In the complete equation of Asano et al. (2013) for the characteristic timescale τ_g , this quantity can be expressed as a function of grain size a , sticking coefficient of refractory elements α and mean velocity of metals in the gas $\langle v \rangle$ as

$$\tau_g = \frac{4\langle a \rangle^3 \rho_d}{3\langle a \rangle^2 \alpha \rho_{\text{ISM}} Z \langle v \rangle}, \quad (17)$$

where $\langle a \rangle^2$ and $\langle a \rangle^3$ are the second and third moment of the grain size distribution, respectively, while ρ_d and ρ_{ISM} are the average dust and ISM mass density. Asano et al. (2013) showed that assuming for the typical molecular cloud temperature a value of 50 K, 100 cm^{-3} for the cloud ambient density and an average value of $0.1 \mu\text{m}$ for the grain size, it is possible to express τ_g as:

$$\tau_g = 2.0 \cdot 10^7 \times \left(\frac{Z}{0.02} \right)^{-1} [\text{yr}], \quad (18)$$

The cold mass fraction X_{cold} is highly uncertain and plays a crucial role in shaping the dust density profiles; therefore, we will test various assumptions for its value. For this quantity we test two constant values, embracing a reasonable range supported by observations and arguments related to the local cold gas budget. The adoption of the low value for X_{cold} is supported by estimates of the dense gas mass fraction in molecular clouds in the Milky Way, performed through observations of the 1.1 mm dust continuum emission (Battisti & Heyer 2014). In this work, observations of high column density subregions indicate mass fractions as low as 0.07, to be regarded

as upper limits to the true mass fractions. Motivated by these results, we assume for our model a value of $X_{\text{cold}} = 0.05$ (Model 1 of Tab. 2).

A larger value for X_{cold} can be derived instead from estimates of the local budget of neutral and molecular gas. For the local molecular and neutral comoving gas density, Fukugita & Peebles (2004) report estimates $\Omega_{\text{H}_2} = 1.6 \times 10^{-4}$ and $\Omega_{\text{HI}} = 4.2 \times 10^{-4}$ (expressed as density parameters), respectively. From the ratio between the two, we obtain $X_{\text{cold}} \sim 0.25$ (Model 2).

As third option, for X_{cold} we assume the profile derived for M74 as a function of the galactocentric radius (Model 3), expressed as

$$X_{\text{cold}}(R) = \frac{M_{\text{H}_2}(R)}{M_{\text{H}_2}(R) + M_{\text{HI}}(R)}, \quad (19)$$

where $M_{\text{HI}}(R)$ and $M_{\text{H}_2}(R)$ are the mass of HI and H2 observed in M74, respectively, at the radius R . The adopted prescriptions for dust accretion are shown in the left panel of Fig. 7, whereas in the right panel we show the prescriptions for dust destruction.

As for the dust destruction, the most crucial parameter is the ISM mass cleared out of dust that, in the formulation of Asano et al. (2013), can be expressed as:

$$M_{\text{clear}} = 1535 n_{\text{ISM}}^{-0.2} \cdot (Z/Z_{\odot} + 0.039)^{-0.289} [M_{\odot}], \quad (20)$$

and depends on the ISM particle density n_{ISM} and on the metallicity of the gas Z . The idea behind a metal-dependent cleared mass is that gas cooling is a function of metallicity, in that metal-poor gas cools less efficiently, thus remaining at high temperatures for longer, increasing the amount of dust destroyed by thermal sputtering in shocked gas (Priestley et al. 2022). As for the density, for our purposes it is convenient to assume an average value, i.e. $n_{\text{ISM}} = 1 \text{ cm}^{-3}$ (Gioannini et al. 2017b), corresponding to the average interstellar density of the Galaxy (Ferrière 1998). The prescriptions adopted for M_{clear} are summarised in the right panel of Fig. 7.

As visible in the upper panel of Fig. 8, all these assumptions lead to similar results, i.e. an overestimate of the dust density profile at small radii, i.e. at $R < 7 \text{ kpc}$, with noticeable differences only in the outermost regions, where the metallicity is lower than in the centre, and therefore the dust destruction timescale is the smallest in the whole galaxy.

The three assumptions for the cold mass fraction imply a factor ~ 3 overestimation of the overall dust budget detected in M74.

We now focus on one single model for dust accretion, where for the cold gas fraction we assume the 'cosmic' average value of $X_{\text{cold}} = 0.25$ and test different assumptions regarding destruction, by adopting various prescriptions for the cleared mass M_{clear} .

In the recent work of Priestley et al. (2022), the effective mass cleared of dust is expressed as:

$$M_{\text{clear}} = \frac{8143}{1 + Z/(0.14Z_{\odot})} [M_{\odot}]. \quad (21)$$

We note that in Eq. (21), the dependence of M_{clear} on the metallicity is stronger than as prescribed by Asano et al. (2013) (see the right panel of Fig. 7). According to Priestley et al. (2022), Eq. 21 might overestimate the metallicity dependence of M_{clear} by neglecting kinetic sputtering, at variance with other authors that include this process (Yamasawa et al. 2011). The results obtained adopting Eq. (21) (Model 4) are shown in the top panel of Fig. 8 as dashed lines.

The adoption of these prescriptions do not lead to any significant improvement, as the observed inner dust profile is still overestimated. This is the effect of a significant metal production occurring in the innermost regions, that leads to a reduced value of M_{clear} and therefore inefficient dust destruction. The large dust densities obtained at the innermost radii thus indicate that the models underestimate dust

Table 2. Models investigated in this work. First column: model number; second column: adopted stardust prescriptions; third column: dust destruction model; fourth column: adopted dust accretion prescriptions.

MODEL	Stardust prescriptions	Destruction	Accretion
1	D17 (AGB), B07 (SNe)	Asano et al. (2013) (M_{clear} : Eq. 20)	Asano et al. (2013) ($X_{\text{cold}} = 0.05$)
2	D17 (AGB), B07 (SNe)	Asano et al. (2013) (M_{clear} : Eq. 20)	Asano et al. (2013) ($X_{\text{cold}} = 0.25$)
3	D17 (AGB), B07 (SNe)	Asano et al. (2013) (M_{clear} : Eq. 20)	Asano et al. (2013) (variable X_{cold})
4	D17 (AGB), B07 (SNe)	Priestley et al. (2022) (M_{clear} : Eq. 21)	Asano et al. (2013) ($X_{\text{cold}} = 0.25$)
5	D17 (AGB), B07 (SNe)	Temim et al. (2015) (M_{clear} : $4000 M_{\odot}$)	Asano et al. (2013) ($X_{\text{cold}} = 0.25$)
5'	D17 (AGB), B07 (SNe)	Temim et al. (2015) (M_{clear} : $2667 M_{\odot}$ at $R = 1$ kpc; $4000 M_{\odot}$ at $R > 1$ kpc)	Asano et al. (2013) ($X_{\text{cold}} = 0.25$)
6	D17 (AGB), B07 (SNe)	Asano et al. (2013) (M_{clear} : Eq. 20)	Mattsson et al. (2012) ($\xi = 500$)
7	D17 (AGB), B07 (SNe)	Priestley et al. (2022) (M_{clear} : Eq. 21)	Mattsson et al. (2012) ($\xi = 500$)
8	D17 (AGB), B07 (SNe)	Asano et al. (2013) (M_{clear} : Eq. 20)	Mattsson et al. (2012) ($\xi = 225\nu$)
9	D17 (AGB), B07 (SNe)	Asano et al. (2013) (M_{clear} : Eq. 20)	Mattsson et al. (2012) ($\xi = 150/\nu$)
9'	D17 (AGB), B07 (SNe)	Asano et al. (2013) (M_{clear} : $2/3$ of Eq. 20 at $R=1$ kpc; Eq. 20 at $R > 1$ kpc)	Mattsson et al. (2012) ($\xi = 150/\nu$)

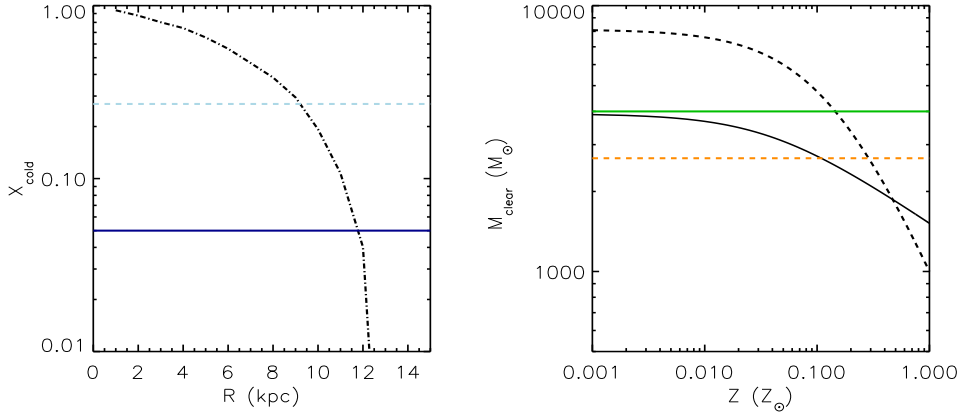


Figure 7. Summary of the adopted prescriptions for dust accretion and destruction. Left panel: cold gas fraction X_{cold} as a function of galactocentric radius as in Eq. 19 (black dash-dotted line) and constant, with a value of 0.05 (blue solid line) and 0.25 (light-blue dashed line). Right panel: interstellar mass cleared out of dust M_{clear} from Asano et al. (2013) (black solid line), from Priestley et al. (2022) (black dashed line) and constant with a value $4000 M_{\odot}$ (green solid line) and of $2667 M_{\odot}$ (corresponding to $2/3$ or the previous value, orange dashed line) as adopted in the innermost regions (see Sect. 4.3.2).

destruction, i.e. that the prescriptions adopted so far for M_{clear} are inadequate. To solve this conundrum, in the following we will test another possibility.

The work of Temim et al. (2015) includes the analysis of more than 80 SN remnants (SNR) in the Magellanic Clouds, in which the destroyed dust masses were determined by means of multiwavelength observations. In particular, the sizes of the SNR were determined by means of X-ray data, whereas IR spectra obtained with Herschel enabled to estimate of the dust mass by means of two-component SED fitting, including silicate and carbon dust. For the total effective swept-up mass of dust, Temim et al. (2015) suggest a weak dependence on ISM density. This weak dependence on the ISM density is due to the fact that the dust mass destroyed by SNR is mostly determined by the dust-to-gas value in the pre-shocked ISM. The typical values for the cleared (or swept-up) mass values derived by Temim et al. (2015) for carbon dust and silicates are of the order of $\sim 2000 M_{\odot}$. However, in the pre-shocked ISM around the studied SNR, Temim et al. (2015) measure dust-to-gas (DGR) ratios that are a factor of two to three higher than the average DGR galactic values. Considering that $G_i = G_{i,d}/\text{DGR}$, in our equations (e. g.,

eq. 10) we take into account an enhanced DGR around SN remnants by assuming a factor two larger cleared mass. Temim et al. (2015) also suggest a weak dependence on metallicity of the swept-up mass, $M_{\text{clear}} \propto \zeta_m^{-0.15}$, where ζ_m is the metallicity normalized to its solar value, and taken to be equal to 0.3 for the Magellanic Clouds.

Based on these results, we examine the effects of a constant value for M_{clear} , i.e. independent on both density and metallicity, and assume $M_{\text{clear}} = 4000 M_{\odot}$ (Model 5), therefore larger than the average cleared dust mass derived in SNR by Temim et al. (2015). The results of this assumption are shown by the dash-dotted profile in the bottom panel of Fig. 8, that outline the significant improvement in accounting for the observed profiles with respect to the previous prescriptions at all radii, but in the innermost regions, i.e. at $R < 2$ kpc. This is due to the larger SFR, and therefore CC SN rate in the inner annulus ($R \sim 1$ kpc), by a factor ~ 3 larger than the values at 2 kpc.

4.3.2 Mattsson et al. (2012) prescriptions for accretion

Dwek (1998) expressed the rate per unit volume at which the dust

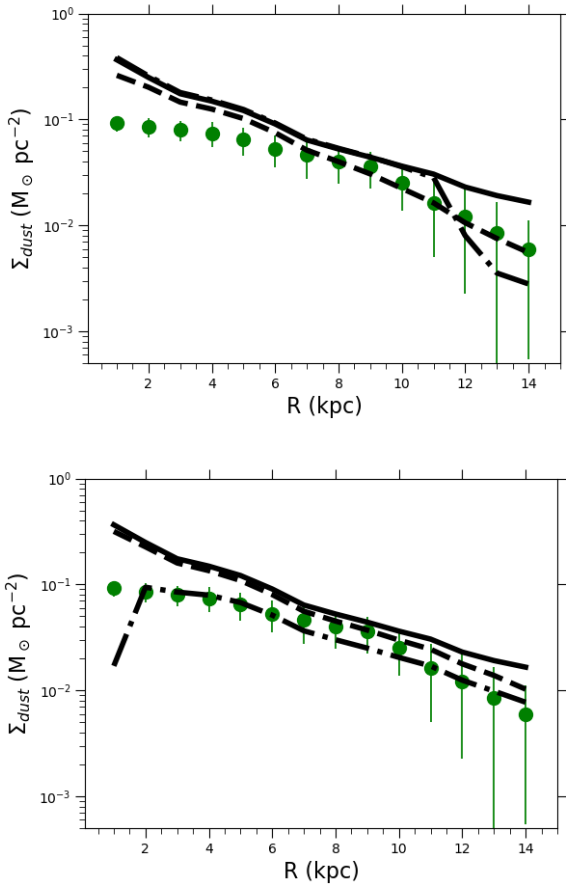


Figure 8. Σ_{dust} as function of galactocentric radius observed in M74 (green circles) and computed adopting the prescriptions of [Asano et al. \(2013\)](#) for dust accretion and testing different timescales for dust destruction. The top panel shows the effects of three different choices for the adopted cold gas fraction X_{cold} , i.e. $X_{\text{cold}} = 0.05$ (black dashed line, Model 1 of table 2), $X_{\text{cold}} = 0.25$ (black solid line, Model 2), and a variable X_{cold} (Model 3) at different radii and computed as described in Sect. 4.3.1 (dash-dotted line). In the bottom panel, the results of a model with $X_{\text{cold}} = 0.25$ and different prescriptions for the cleared mass M_{clear} are shown, i.e. the one from [Asano et al. \(2013\)](#) (black solid line, Model 2), [Priestley et al. \(2022\)](#) (dashed line, Model 4), and [Temim et al. \(2015\)](#) (dash-dotted line, model 5).

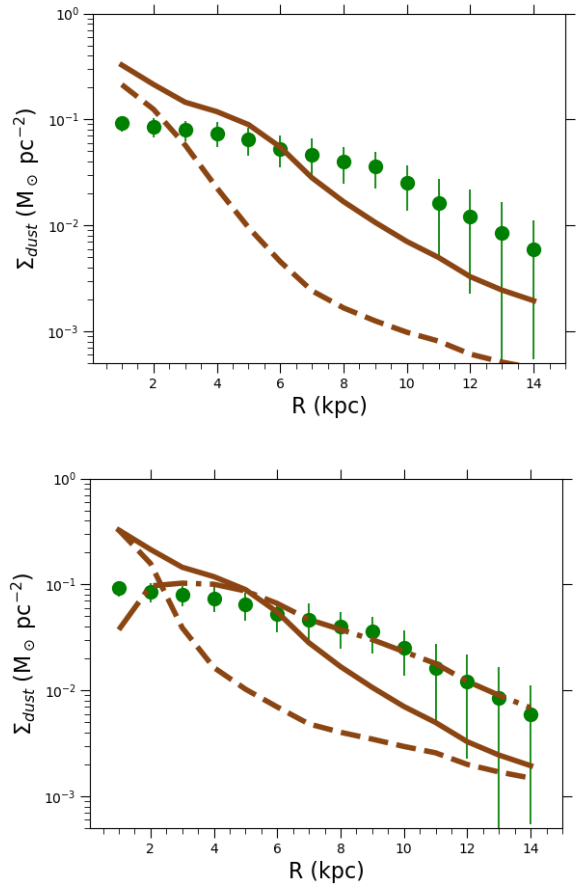


Figure 9. Σ_{dust} as function of galactocentric radius observed in M74 (green circles) and computed adopting the prescriptions of [Mattsson et al. \(2012\)](#) for dust accretion and testing different timescales for dust destruction. In the top panel, we show the results obtained assuming the [Asano et al. \(2013\)](#) (Model 6, brown solid line) and [Priestley et al. \(2022\)](#) (Model 7, brown dashed line) prescriptions for the cleared mass M_{clear} and a constant value (500) for the parameter ξ of Eq. 23. In the bottom panel, we show the effects of different choices for the parameter ξ as a function of the SF efficiency ν . Brown solid line: constant value for ξ ($\xi = 500$, Model 6); brown dashed line: $\xi = 225 \nu$ (Model 8); brown dash-dotted line: $\xi = 150/\nu$ (Model 9). In each model, the adopted M_{clear} is from [Asano et al. \(2013\)](#). The solid green circles are as in Fig. 1.

grains grow by accretion of metals for the element A

$$\frac{dN_A}{dt} = \alpha \pi a^2 n_g(A) n_{\text{gr}} \bar{v}, \quad (22)$$

where α is the sticking coefficient of element A to the dust grain, n_g and n_{gr} are the number density of gas particles and dust grains, respectively, and $\bar{v} = \frac{8kT}{\pi m_A}$ is the mean thermal speed of atoms with mass m_A in interstellar gas with temperature T . By expressing Eq. 22 in terms of dust, cold gas and metal surface densities, [Mattsson et al. \(2012\)](#) showed that τ_0 can be written as:

$$\tau_0 = \frac{\Sigma_{\text{gas}}(t)}{\xi Z \dot{\Sigma}_*(t)}, \quad (23)$$

where Σ_{gas} is the gas surface density, $\dot{\Sigma}_*(t)$ is the SFR density and ξ is a free parameter, whose expected value is of the order of a few hundred, required to obtain $\tau_0 \sim 10^7$ yr for a solar metallicity and values of Σ_{gas} and $\dot{\Sigma}_*(t)$ observed in the solar neighbourhood. In this case, it is first convenient to adopt a fixed value of $\xi = 500$ and test

various assumptions for M_{clear} . The results are shown in the top panel of Fig. 9, where we see that the adoption of both the [Asano et al. \(2013\)](#) and [Priestley et al. \(2022\)](#) prescriptions for M_{clear} produce too steep dust mass profiles with respect to observations. We have tested also the adoption of the [Temim et al. \(2015\)](#) prescriptions for M_{clear} (not shown in the plot), finding no substantial improvement in reproducing the observed profile.

One possible way to reduce the slope in the predicted dust profile is to adopt a variable ξ parameter as a function of galactocentric distance. To this aim, we will test a couple of different parametrisations in which ξ will be expressed as a function of the SF efficiency ν , represented by a decreasing function of radius as shown in Fig. 3. This will require sticking to one particular prescription for destruction, for which we adopt the [Asano et al. \(2013\)](#) formula for M_{clear} (Eq. 20).

In our first attempt, we assume ξ as a linear function of the SF

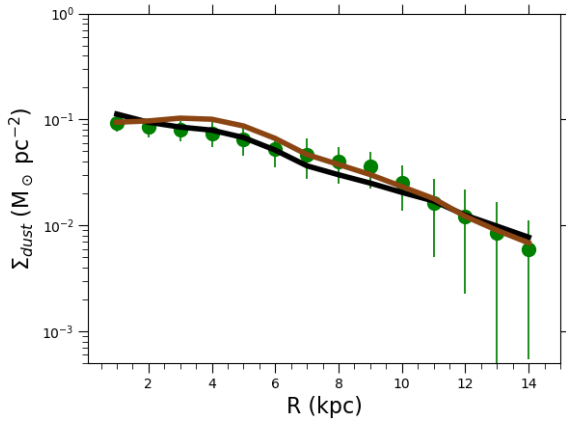


Figure 10. Best models obtained assuming the [Asano et al. \(2013\)](#) (black solid line, Model 5' of Tab.2) and [Mattsson et al. \(2012\)](#) (brown solid line, Model 9' of Tab.2) prescriptions for dust accretion. In both models, the adopted M_{clear} has been reduced by a factor of 1/3 in the innermost regions ($R < 2$ kpc) to reproduce the dust mass density observed at $R = 1$ kpc in the M74 galaxy. The solid green circles are as in Fig. 1.

efficiency ν :

$$\xi = K\nu \quad (24)$$

For the proportionality factor K , in the bottom panel of Fig. 9 we show the results obtained assuming $K = 225$ (Model 7). However, the adoption of other values within the same order of magnitude does not lead to significantly different results. This model is represented by the dashed line, showing a flatter profile at outer radii ($R > 4$ kpc) than the model with constant ξ (solid line), resulting from a decreased accretion rate (due to longer SF timescales) in the outer regions, in strong disagreement with the observed profile.

Conversely, the assumption of ξ inversely proportional to ν

$$\xi = K'/\nu \quad (25)$$

leads to reproduce satisfactorily the slope of the observed profile, as shown by the dash-dotted line in the bottom panel of Fig. 9. In this case, the proportionality constant of Eq. 25 is set to $K'=150$, a value optimised to reproduce also the normalisation of the observed profile, that in this case is the dust surface density at $R=2$ kpc. As in the case of the best model obtained with the [Asano et al. \(2013\)](#) prescriptions for dust accretion, the latter assumption does not allow us to account for the dust density in the innermost regions, i.e. at $R=1$ kpc, where the amount of dust is underestimated. This is due to a very high destruction rate in the innermost regions, that stems from the high star formation rate, thus implying a too high SN rate.

Fig. 10 shows the results of the two best models 5' and 9', in which the dust density is reproduced at all radii, including also the inner region ($R=1$ kpc). In both models, the dust destruction rate has been reduced by a factor of 1/3 to increase the final dust mass. Although in our model this assumption is performed ad-hoc and on an empirical basis, it has interesting implications and motivated physical grounds, discussed in Sect. 4.4.

4.3.3 Dust-to-gas and Dust-to-stellar ratios

By construction, the final DGR and dust-to-stellar (DSR) ratios obtained with our best models match the values observed in M74. Here we discuss the predicted DGR and DSR as a function of metallicity,

galactocentric distance and compare our results with the integrated values observed in other DustPedia galaxies. The sample we consider in our analysis includes a sub-set of late- and early-type spiral galaxies for which the metallicity (expressed as $12+\log(\text{O}/\text{H})$), total dust, gas and stellar mass have been measured and is composed of 393 galaxies in total (163 early-type and 230 late-type spirals).

For details on how the measurements were performed and the data collected, we refer the reader to [Casasola et al. \(2017\)](#) and [Casasola et al. \(2020\)](#). The DGR as a function of metallicity is presented in Fig. 11, in which the results of Model 5' (9') is reported in the left (right) panel. In both cases, the model values computed at the final time are in excellent agreement with the data for the sub-sample of late-type galaxies. The curves of different colors describe the evolution at 4 representative radii, from 3 kpc to 12 kpc. Isochrones have been plotted for both model sets, computed at three different evolutionary times (1 Gyr, 5 Gyr and 10 Gyr, dashed lines), useful to examine the evolution of the DGR at different radii. As for Model 5', the slope of the isochrones at the outer radii ($R > 8$ kpc) progressively steepen with time, indicating that also the DGR gradient steepens appreciably at late evolutionary stages (≥ 10 Gyr). This occurs because of the dependence of the accretion timescale τ_g on metallicity (Eq. 18), leading to longer timescales in more external regions as due to longer infall and SF timescales.

Less differences are visible in the evolution of the DGR at $R < 6$ kpc, characterised by a flatter behaviour of the isochrones at times ≤ 10 Gyr and a flatter gradient at the final time than the outer regions.

At the final time, the track computed at the inner radius overlaps with the DGR observed in early-type spirals, presenting values comparable to late-type galaxies but characterised by larger metallicities. The tracks of Model 9' (right panel of Fig. 11) are steeper than Model 5' and show a stronger evolution, visible in the larger DGR ratios at various radii at 1 and 5 Gyr.

The total DSR of the models is ~ 0.001 , in good agreement with the values measured in late spirals of the DustPedia sample. The evolution of the DSR at different galactic radii is shown in Fig. 12, in which the results of models 5' and 9' are reported in the left and right panels, respectively, compared to the local values observed in DustPedia galaxies (open circles). In this case, the behaviour of the isochrones is the inverse of the DGR, in that they steepen at lower radii, specifically decreasing as a function of radius, remaining approximately flat at $R > 6$ kpc. This is due to the shape of the stellar mass profile, particularly steep at small radii (< 3 kpc), where the dust mass profile is essentially flat (see Fig. 1). The final values of the model at different radii are in good agreement with the values observed in late-type DustPedia galaxies. The end-point of the track at $R=2$ kpc overlaps with the DSR of the lowest mass early type spirals, presenting $\text{DSR} \gtrsim 3 \times 10^{-4}$.

The evolution of Model 9' at various radii is different than the one of Model 5', in that the tracks of the former present a flatter early evolution with metallicity and they evolve more closely, presenting a significantly smaller range of DSR at 5 Gyr. At later times, the two models show little differences. The closer evolution of the tracks of Model 5' and 9' at late evolutionary times are visible also in Fig. 13, in which we show the dust-to-baryon ratio computed at various radii as a function of the gas fraction. The analysis of this quantity outlines the steeper growth of the tracks of Model 9', that at 5 Gyr show $\text{DBR} > 1 \times 10^{-4}$, whereas at the same time, Model 5' shows still DBR values of a few $\times 10^{-5}$ at all radii.

Moreover, this plot emphasises the separation between DustPedia late- and early-types, with the latter presenting in most cases lower gas fractions (≤ 0.2) than the former. In their later stages, i.e. at evolutionary times > 10 Gyr, the theoretical tracks of the innermost

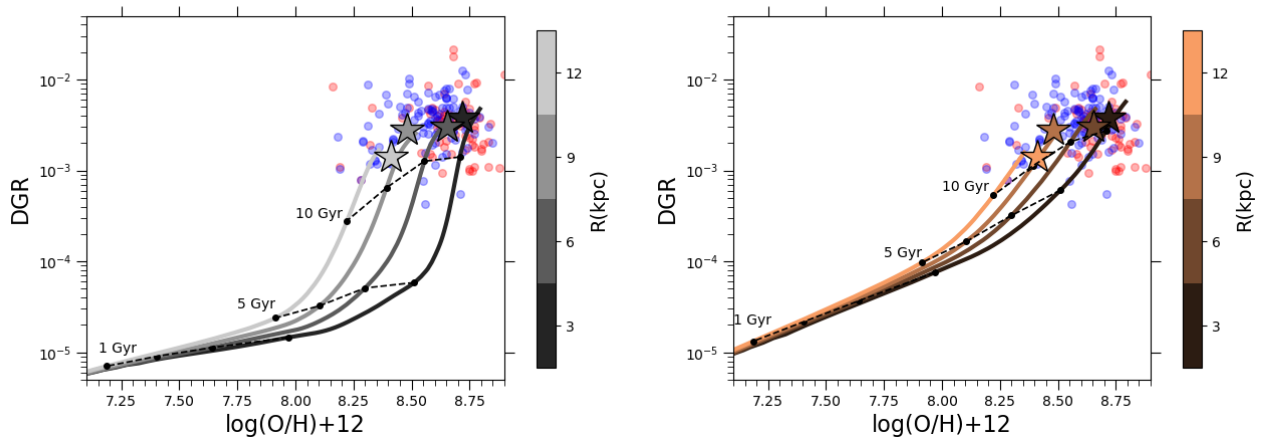


Figure 11. Dust-to-gas ratio (DGR) as a function of $\log(\text{O}/\text{H})+12$ for the best models at different galactocentric radii. Left panel: best model obtained assuming the Asano et al. (2013) dust accretion prescriptions (Model 5' of Tab 2). The black, dark grey, grey and light grey curves represent the evolutionary tracks at radii 3 kpc, 6 kpc, 9 kpc and 12 kpc, respectively. The stars represent the values measured in M74. The red and blue circles are the DGR values observed in early-type (red) and late-type (blue) spiral galaxies of the DustPedia sample. The dashed lines are isochrones at 1 Gyr, 5 Gyr and 10 Gyr. Right panel: best model obtained assuming the Mattsson et al. (2012) dust accretion prescriptions (Model 9' of Tab 2). The dark brown, brown, light brown and orange curves represent the evolutionary tracks at radii 3 kpc, 6 kpc, 9 kpc and 12 kpc, respectively. The other symbols and lines are as in the left panel.

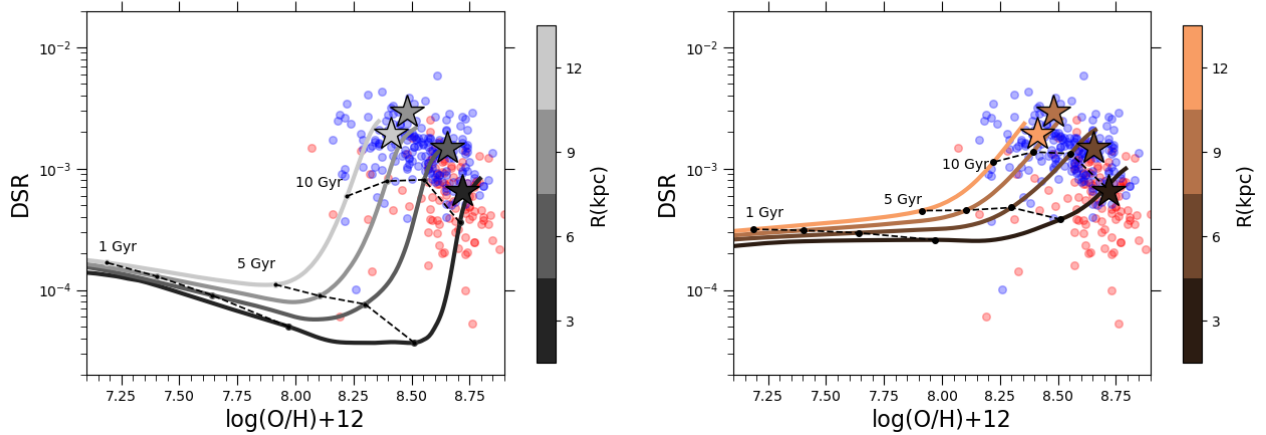


Figure 12. Dust-to-star ratio (DSR) as function of $\log(\text{O}/\text{H})+12$ for the best models at different galactocentric radii. Left panel: best model obtained assuming the Asano et al. (2013) dust accretion prescriptions (Model 5' of Tab 2). The black, dark grey, grey and light grey curves represent the evolutionary tracks at radii 3 kpc, 6 kpc, 9 kpc and 12 kpc, respectively. Other symbols are as in Fig. 11. Right panel: best model obtained assuming the Mattsson et al. (2012) dust accretion prescriptions (Model 9' of Tab 2). The dark brown, brown, light brown and orange curves represent the evolutionary tracks at radii 3 kpc, 6 kpc, 9 kpc and 12 kpc, respectively. The other symbols and lines are as in the left panel.

radii of models 5' and 9' overlap with the DBR of the local early type-galaxies characterised by larger gas fraction (~ 0.2).

4.4 Discussion

In this work, we figured out simple recipes to model destruction and accretion that can reproduce the observed profile of M74 without any ad-hoc assumption. This holds at all radii except in the innermost regions ($R < 2$ kpc), where we empirically decreased the dust cleared mass to match the observational data. In this section, first we discuss possible physical reasons for this choice and on the possible radial dependence of dust destruction, as a result of a different impact of stellar feedback at different galactic radii.

We are aware that the adopted recipes might not be unique; in

this regard, our study is useful to outline the degeneracy between the main parameters regulating dust destruction and accretion. We also discuss the relative roles of these processes in our models, that are still a matter of debate, and compare our findings with other relevant works.

4.4.1 On the efficiency of dust destruction at different galactic radii

How the destruction of dust depends on the galactocentric radius and, more in general, on the stellar feedback in different environments, is largely unknown. Although a few works dealt with the destruction of dust from single SN (Silvia et al. 2010, Martínez-González et al. 2019), the destruction of dust from multiple supernovae has rarely been treated. In a multiphase ISM, it is known that the destruction is

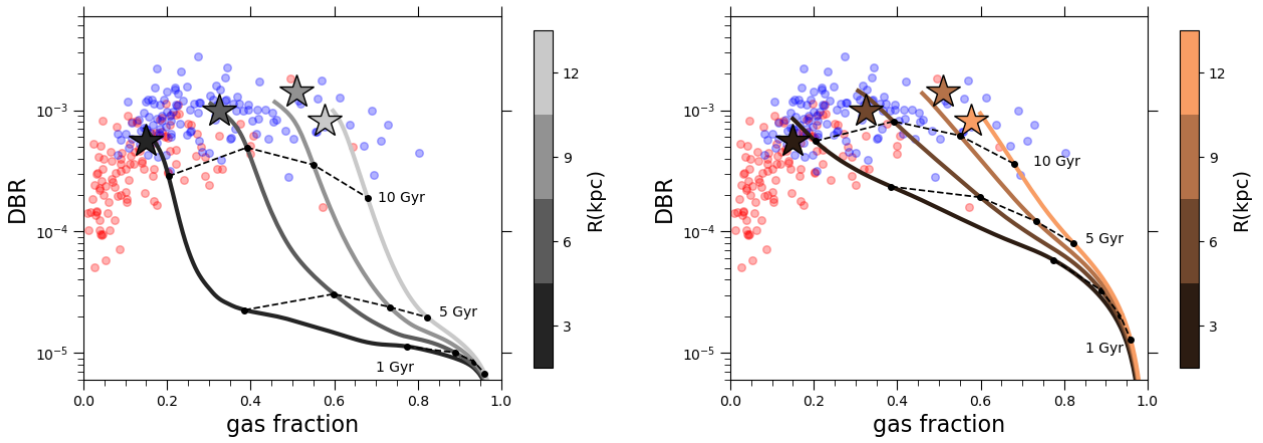


Figure 13. Dust-to-baryon ratio (DBR) as function of the gas fraction for the best models at different galactocentric radii. Left panel: best model obtained assuming the [Asano et al. \(2013\)](#) dust accretion prescriptions (Model 5' of Tab 2). The black, dark grey, grey and light grey curves represent the evolutionary tracks at radii 3 kpc, 6 kpc, 9 kpc and 12 kpc, respectively. Right panel: best model obtained assuming the [Mattsson et al. \(2012\)](#) dust accretion prescriptions (Model 9' of Tab 2). The dark brown, brown, light brown and orange curves represent the evolutionary tracks at radii 3 kpc, 6 kpc, 9 kpc and 12 kpc, respectively. The other symbols and lines are as in Fig. 11.

related to the mass exchange between the hot and cold media ([McKee 1989](#); [Peters et al. 2017](#)). Such exchange determines the circulation of gas from the warm neutral medium, where dust abundances are reduced by destruction in interstellar shocks generated by massive stellar feedback, and matter enriched with dust due to accretion on grain surfaces at higher gas densities. In this context, the knowledge of the filling factor of the warm and hot medium driven by pre-SNe and SN feedback and its dependence on the environment is fundamental. Such quantity is determined by mutual interactions of SN remnants at various radii and their impact on the multiphase medium, that has instead already been treated in various works.

In the innermost regions of galactic discs, the evolution of SN remnants might indeed be different than at outer radii. [Yalinewich et al. \(2017\)](#) showed that at small distances from the Galactic Centre, SN remnants evolve differently than at outer radii because of the higher abundance of young massive stars. These stars continuously emit stellar winds with total mass loss rate of $\sim 10^{-3} M_{\odot}/\text{yr}$ and propagating with typical velocity of $\sim 700 \text{ km/s}$ ([Rockefeller et al. 2004](#)). Instead of a static, uniform density medium, a SN exploding near the Galactic center propagates into a continuously wind-swept environment and a steep density profile, causing a non-spherical expansion of the SN remnant [Rimoldi et al. \(2015\)](#), due to a faster deceleration of the fluid moving towards the centre. This might influence the interactions between different SN bubbles and the impact of stellar feedback.

By means of three-dimensional hydrodynamic simulations of the galactic disc, [Melioli et al. \(2009\)](#) studied the evolution of galactic fountains generated by stellar OB associations at various galactocentric distances, in a model that includes differential galactic rotation and a gaseous halo. The energy restored by OB associations generates several hot cavities in the disc, whose lifetime and overlapping are determined by the duration of SN activity, local density and rotation. These factors strongly influence the filling factor of the hot cavities, that drops sharply towards the smallest galactic radii. This finding is supported also by observations of local galactic discs. In a detailed study of the HI holes in the spiral galaxy NGC 69456, [Boomsma et al. \(2008\)](#) find that the hole covering factor drops sharply towards smallest galactic radii. This effect is ascribed to both a drop of the HI column density and to the stronger shear, shortening the hole life-

times and therefore decreasing their overlapping. [Della Bruna et al. \(2022\)](#) present a study based on the Multi Unit Spectroscopic Explorer (MUSE) of the properties of HII regions in the nearby spiral galaxy M83, aimed at quantifying the effects of stellar feedback in different galactic environments. They compare the internal pressure of HII regions with the environmental pressure, finding that in the innermost regions ($R \leq 0.5 \text{ kpc}$) the latter is almost one order of magnitude higher than the former, indicating that stellar feedback is not sufficient to drive the expansion of the ionised regions. On the other hand, in more external zones, HII regions are over-pressurized, therefore they can expand. This indicates that the strength of early stellar feedback increases at increasing galactic radii.

In this framework, in our model a particularly inefficient destruction at galactic radii $< 1 \text{ kpc}$ might be qualitatively explained by a lesser impact of stellar feedback at small galactocentric distances. To test this hypothesis quantitatively, 3D hydrodynamical simulations of a realistic galactic disc will be required, in which stellar feedback and dust destruction are taken into account.

4.4.2 On the balance between destruction and accretion in galaxies

One often debated aspect in studies of dust evolution concerns which processes among stardust production, accretion and destruction affect most the dust budget in galaxies. In Fig. 14, we show the relative roles of these mechanisms in the best models of our set, i.e. Model 5' and Model 9', through the ratio between the timescales of each processes, both computed at a galactocentric radius $R = 8 \text{ kpc}$, representative of the entire galaxy. The accretion and destruction timescales are defined in Sect. 3.2, whereas the production timescale is the ratio between the cumulative mass of dust and the total stardust production rate, computed including both AGB stars and SNe. In Model 5', the stardust production dominates over accretion and destruction only at early times, i.e. up to $\sim 5 \text{ Gyr}$ and 2 Gyr , respectively. Model 9' has a more prolonged dominion of production by stars, extending up to 6 Gyr and 8 Gyr over accretion and destruction, respectively. Model 5' settles on a quasi-equilibrium between destruction and accretion after 8 Gyr , that continues up to the present time. At a comparable epoch the ratio between the timescales of these processes becomes

approximately constant in Model 9', that also protracts to the present time. However, the two models predict two distinct behaviors regarding the relative roles of dust production and destruction and their evolution, as they settle onto different values of the ratio $\tau_{\text{acc}}/\tau_{\text{destr}}$.

Several models rely on the primary role of accretion in determining the galactic dust budget (e. g., Dwek 1998; Calura et al. 2008; Gall et al. 2011; Valiante et al. 2011; Mattsson et al. 2014). On the other hand, Gall & Hjorth (2018) performed an empirical study of the dust mass in high- and low- z galaxies, in which they explore a simple dust production scenario that applies to star-forming systems. They considered star-forming massive galaxies and local galaxies, including the Milky Way and the Magellanic Clouds, and a wide set of measurements of the dust mass in SNe and SN remnants at various stages. In their study, the observed dust masses can be accounted for by a simple model in which SNe produce the majority of the dust in the current star formation episode, on timescales $\lesssim 10$ -100 Myr. However, their results do not exclude the formation of dust through rapid grain growth out of the metals expelled by massive stars. Rapid destruction and reformation of the dust is also allowed, as long as the two terms are roughly balanced, similar to Model 5'. At the moment it is very difficult to determine which of these possibilities is the most realistic. In fact, the study of the cosmic evolution of the comoving mass density of dust indicates that the destruction must play an important role. This is indicated by the decrease of the dust mass at $z < 2$ (Pozzi et al. 2020), mainly reproduced by models in which the observed decrease of the dust mass is determined by destruction and stardust production has a marginal role at these epochs (Gioannini et al. 2017b). In the framework of our models, in this case the implication is that accretion also must play a primary role in the survival of dust in galaxies.

5 CONCLUSIONS

The DustPedia project offers a wealth of multi-wavelength constraints on a large sample of local galaxies of various morphological types (Davies et al. 2017, 2019; Casasola et al. 2020). In the past, these constraints have been used within a statistical framework, to achieve constraints on chemical and dust evolution parameters for nearby galaxies (De Vis et al. 2021).

In this paper, we introduce a multi-zone chemical evolution model of one DustPedia galaxy, M74, calibrated by means of MCMC methods. For this purpose, we use exquisite, high-resolution data collected to study spatially-resolved fundamental scaling relations (such as the Main Sequence and the Schmidt-Kennicutt law) in disc galaxies (Enia et al. 2020; Morselli et al. 2020; Casasola et al. 2022). We take into account the stellar mass and gas profiles obtained in these studies, and use Bayesian analysis to constrain two fundamental parameters defining the evolution of M74, the accretion timescale τ and the SF efficiency ν , in both cases as a function of galactocentric radius R , defined as the distance between a given annuli and the centre of M74. The best model derived with this method is then used to investigate the dust content of M74, comparing the observed dust density profile with the results of our chemical evolution model. Various prescriptions have been considered for two key parameters, i.e. the typical dust accretion timescale τ_0 and the mass of gas cleared out of dust by a SN remnant, M_{clear} , playing a primary role in regulating the dust growth and destruction rate, respectively. Our results can be summarised as follows.

(i) Our analysis supports an accretion timescale increasing with R , thus supporting an 'Inside-Out' formation for M74. This confirms the result found for the accretion timescale of the Milky Way considering

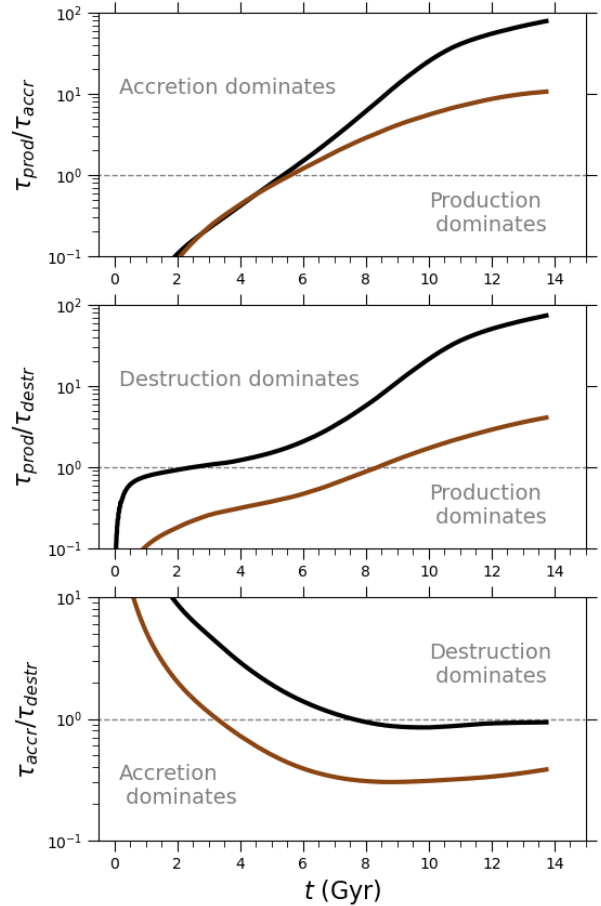


Figure 14. Ratios between accretion, destruction and stardust production timescales for Model 5' (black lines) and Model 9' (brown lines) of Tab 2 as a function of time and at a galactic radius of 8 kpc. Top panel: ratio between stardust production and accretion timescales. Central panel: ratio between stardust production and destruction timescales. Bottom panel: ratio between accretion and destruction timescales. In each panel, the thin, grey dashed line indicates a ratio equal to 1, corresponding to the equilibrium between the two processes.

the spatial dependence of the chemical abundances obtained from various diagnostics, such as the 'G-dwarf' distribution at various galactocentric radii and the abundance gradient, as traced by the gas or young stars (Matteucci & Francois 1989; Romano et al. 2000; Chiappini et al. 2001).

The SF efficiency shows a decreasing trend as a function of radius. This is also consistent with what was found in the Milky Way from the analysis of the observed abundances for various chemical elements (Grisoni et al. 2018, Palla et al. 2020b).

For both quantities, our analysis indicates a weaker radial dependence than in the Milky Way. This implies lesser variations of the gas accretion and SF rates with radius, that could manifest in a lower dispersion of the stellar ages or chemical abundances as a function of radius.

(ii) We have tested the effects of radial gas flows on the observables considered in this work, i.e. the stellar and gas density profiles and the metallicity gradient. We have considered various cases for the most critical quantity characterising this process, i.e. the radial

velocity pattern, including constant and radial-dependent values, by simultaneously considering other assumptions for the radial dependence of the infall and SF law. We have found that even values as low as -0.5 km/s are enough to steepen significantly the metallicity gradient and the gas density profile. By assuming net radial inflows in the galaxy and by varying the prescriptions on the radial dependence of gas accretion and SF, we are not able to reproduce simultaneously the observational constraints of M74, i.e. the stellar density, gas density and metallicity gradient.

(iii) Considering various functional forms for the characteristic dust accretion timescale and the cleared dust mass, we are able to account for the dust mass profiles observed in M74. Our study outlines the degeneracy between the most fundamental accretion and destruction parameters in shaping the interstellar dust content in galaxies, as two models with different prescriptions provide remarkably similar results for dust density profile. These two models envisage a different current balance between destruction and accretion, in that both an equilibrium and a dominion of accretion over destruction can equally reproduce the available constraints. On much larger scales, a scenario in which destruction plays a marginal role seems perhaps excluded by the observed decreasing evolution of the comoving dust mass density, difficult to account for by means of astration only.

(iv) Despite their degeneracy, both the two best models obtained here can reproduce the observed dust density profile at all radii except in the innermost regions ($R < 2$ kpc), where the dust content is underestimated. In both cases, the dust destruction rate has to be reduced by a factor of $1/3$ to increase the dust mass observed in the most central regions of M74. A particularly inefficient destruction at small galactic radii < 1 kpc can be qualitatively explained by a lesser impact of stellar feedback at small galactocentric distances. This is supported by studies performed with hydrodynamical simulations of a MW-analog, showing that filling factor of the hot cavities generated by OB stars drops sharply towards the smallest galactic radii (Melioli et al. 2009) and is confirmed also by observational studies of the spatial distribution of HII regions in local discs (Della Bruna et al. 2022).

Although the results presented in this work can be improved in various aspects, our aim is to deliver a model that accounts for the star formation history of the Dustpedia galaxy M74, whose reliability has been assessed on a quantitative basis, using a parametric approach and considering a pre-determined set of observational constraints. This aim is complementary to the ones of other models, such as cosmological ones, in which it is more difficult to tailor a model to a specific system that accurately accounts for observables such as gas and stellar density profiles. In the future, we plan to use the methods described in this paper to extend our study to more Dustpedia galaxies, in order to derive fundamental constraints on their star formation history and the evolution of their dust content. This will lead to significant progress in our understanding of galactic evolution, outlining further the roles played by the most fundamental parameters that regulate it and the differences between individual galaxies.

DATA AVAILABILITY

The data underlying this article are available from the corresponding author, upon reasonable request.

ACKNOWLEDGEMENTS

An anonymous referee is acknowledged for useful suggestions. We acknowledge financial support from grant PRIN MIUR 20173ML3WW_001. FC also acknowledges support from PRIN INAF 1.05.01.85.01. MP acknowledges funding support from ERC starting grant 851622 DustOrigin and computing resources from the “accordo quadro MoU per lo svolgimento di attività congiunta di ricerca nuove frontiere in astrofisica: HPC e data exploration di nuova generazione” between CINECA and INAF. MP also thanks Ilse De Looze, Monica Relaño and Stefan Van der Giessen for the fruitful discussions. VC, SB and FP acknowledge funding from the INAF Main Stream 2018 program “Gas-DustPedia: A definitive view of the ISM in the Local Universe”. FC, VC, SB and FP acknowledge funding from the INAF Mini Grant 2022 program “Face-to-Face with the Local Universe: ISM’s Empowerment (LOCAL)”.

REFERENCES

- Aoyama S., Hou K.-C., Hirashita H., Nagamine K., Shimizu I., 2018, *MNRAS*, **478**, 4905
- Asano R. S., Takeuchi T. T., Hirashita H., Inoue A. K., 2013, *Earth, Planets and Space*, **65**, 213
- Battisti A. J., Heyer M. H., 2014, *ApJ*, **780**, 173
- Baugh C. M., 2006, *Reports on Progress in Physics*, **69**, 3101
- Berta S., et al., 2013, *A&A*, **555**, L8
- Bianchi S., Schneider R., 2007, *MNRAS*, **378**, 973
- Bianchi S., et al., 2018, *A&A*, **620**, A112
- Bianchi S., et al., 2022, *A&A*, **664**, A187
- Bigiel F., Leroy A., Walter F., Brinks E., de Blok W. J. G., Madore B., Thornley M. D., 2008, *AJ*, **136**, 2846
- Bilitewski T., Schönrich R., 2012, *MNRAS*, **426**, 2266
- Boomsma R., Oosterloo T. A., Fraternali F., van der Hulst J. M., Sancisi R., 2008, *A&A*, **490**, 555
- Brook C. B., et al., 2011, *MNRAS*, **415**, 1051
- Bruzual G., Charlot S., 2003, *MNRAS*, **344**, 1000
- Calura F., Menci N., 2009, *MNRAS*, **400**, 1347
- Calura F., Pipino A., Matteucci F., 2008, *A&A*, **479**, 669
- Calura F., Pipino A., Chiappini C., Matteucci F., Maiolino R., 2009, *A&A*, **504**, 373
- Casasola V., Hunt L., Combes F., García-Burillo S., 2015, *A&A*, **577**, A135
- Casasola V., et al., 2017, *A&A*, **605**, A18
- Casasola V., et al., 2020, *A&A*, **633**, A100
- Casasola V., et al., 2022, arXiv e-prints, p. arXiv:2210.15993
- Charlot S., Fall S. M., 2000, *ApJ*, **539**, 718
- Chiappini C., Matteucci F., Romano D., 2001, *ApJ*, **554**, 1044
- Christensen C. R., Davé R., Brooks A., Quinn T., Shen S., 2018, *ApJ*, **867**, 142
- Clark C. J. R., et al., 2018, *A&A*, **609**, A37
- Colavitti E., Matteucci F., Murante G., 2008, *A&A*, **483**, 401
- Colavitti E., Cescutti G., Matteucci F., Murante G., 2009, *A&A*, **496**, 429
- Corwin Harold G. J., Buta R. J., de Vaucouleurs G., 1994, *AJ*, **108**, 2128
- Côté B., Ritter C., O’Shea B. W., Herwig F., Pignatari M., Jones S., Fryer C. L., 2016, *ApJ*, **824**, 82
- Davé R., Finlator K., Oppenheimer B. D., 2011, *MNRAS*, **416**, 1354
- Davies J. I., et al., 2017, *PASP*, **129**, 044102
- Davies J. I., et al., 2019, *A&A*, **626**, A63
- Dayal P., et al., 2022, *MNRAS*, **512**, 989
- De Looze I., et al., 2020, *MNRAS*, **496**, 3668
- De Vis P., et al., 2017, *MNRAS*, **471**, 1743
- De Vis P., et al., 2019, *A&A*, **623**, A5
- De Vis P., Maddox S. J., Gomez H. L., Jones A. P., Dunne L., 2021, *MNRAS*, **505**, 3228
- Dell’Agli F., García-Hernández D. A., Schneider R., Ventura P., La Franca F., Valiante R., Marini E., Di Criscienzo M., 2017, *MNRAS*, **467**, 4431
- Della Bruna L., et al., 2022, *A&A*, **663**, C2

- Di Teodoro E. M., Peek J. E. G., 2021, *ApJ*, **923**, 220
- Dunkley J., Bucher M., Ferreira P. G., Moodley K., Skordis C., 2005, *MNRAS*, **356**, 925
- Dwek E., 1998, *ApJ*, **501**, 643
- Elbaz D., et al., 2007, *A&A*, **468**, 33
- Enia A., et al., 2020, *MNRAS*, **493**, 4107
- Ferrière K., 1998, *ApJ*, **503**, 700
- Foreman-Mackey D., Hogg D. W., Lang D., Goodman J., 2013, *PASP*, **125**, 306
- François P., Matteucci F., Cayrel R., Spite M., Spite F., Chiappini C., 2004, *A&A*, **421**, 613
- Fukugita M., Peebles P. J. E., 2004, *ApJ*, **616**, 643
- Gall C., Hjorth J., 2018, *ApJ*, **868**, 62
- Gall C., Hjorth J., Andersen A. C., 2011, *A&ARv*, **19**, 43
- Gavilan L., Lemaire J. L., Vidalí G., Sabri T., Jæger C., 2014, *ApJ*, **781**, 79
- Gioannini L., Matteucci F., Vladilo G., Calura F., 2017a, *MNRAS*, **464**, 985
- Gioannini L., Matteucci F., Calura F., 2017b, *MNRAS*, **471**, 4615
- Gjergo E., Granato G. L., Murante G., Ragone-Figueroa C., Tornatore L., Borgani S., 2018, *MNRAS*, **479**, 2588
- Goodman J., Weare J., 2010, *Communications in Applied Mathematics and Computational Science*, **5**, 65
- Gould R. J., Salpeter E. E., 1963, *ApJ*, **138**, 393
- Granato G. L., et al., 2021, *MNRAS*, **503**, 511
- Grisoni V., Spitoni E., Matteucci F., 2018, *MNRAS*, **481**, 2570
- Gruppioni C., et al., 2013, *MNRAS*, **432**, 23
- Gusev A. S., Egorov O. V., Sakhibov F., 2014, *MNRAS*, **437**, 1337
- Henriques B. M. B., Thomas P. A., Oliver S., Roseboom I., 2009, *MNRAS*, **396**, 535
- Hirashita H., Kuo T.-M., 2011, *MNRAS*, **416**, 1340
- Ho S. H., Martin C. L., Turner M. L., 2019, *ApJ*, **875**, 54
- Hopkins P. F., et al., 2023, *arXiv e-prints*, p. [arXiv:2301.08263](https://arxiv.org/abs/2301.08263)
- Hou K.-C., Aoyama S., Hirashita H., Nagamine K., Shimizu I., 2019, *MNRAS*, **485**, 1727
- Inoue A. K., 2011, *Earth, Planets and Space*, **63**, 1027
- Iwamoto K., Brachwitz F., Nomoto K., Kishimoto N., Umeda H., Hix W. R., Thielemann F.-K., 1999, *ApJS*, **125**, 439
- Jones A. P., Tielens A. G. G. M., Hollenbach D. J., 1996, *ApJ*, **469**, 740
- Kampakoglou M., Trotta R., Silk J., 2008, *MNRAS*, **384**, 1414
- Kennicutt Robert C. J., 1998, *ApJ*, **498**, 541
- Kewley L. J., Ellison S. L., 2008, *ApJ*, **681**, 1183
- Khoperskov S. A., Vasiliev E. O., 2017, *MNRAS*, **468**, 920
- Konstantopoulou C., et al., 2022, *A&A*, **666**, A12
- Lacey C. G., Fall S. M., 1985, *ApJ*, **290**, 154
- Leroy A. K., et al., 2009, *AJ*, **137**, 4670
- Maiolino R., Mannucci F., 2019, *A&ARv*, **27**, 3
- Mancini M., Schneider R., Graziani L., Valiante R., Dayal P., Maio U., Ciardi B., Hunt L. K., 2015, *MNRAS*, **451**, L70
- Marinacci F., Pakmor R., Springel V., 2014, *MNRAS*, **437**, 1750
- Martínez-González S., Wünsch R., Silich S., Tenorio-Tagle G., Palouš J., Ferrara A., 2019, *ApJ*, **887**, 198
- Martínez-González S., Silich S., Tenorio-Tagle G., 2021, *MNRAS*, **507**, 1175
- Matteucci F., 2012, *Chemical Evolution of Galaxies*, doi:[10.1007/978-3-642-22491-1](https://doi.org/10.1007/978-3-642-22491-1).
- Matteucci F., 2021, *A&ARv*, **29**, 5
- Matteucci F., François P., 1989, *MNRAS*, **239**, 885
- Mattsson L., Andersen A. C., Munkhammar J. D., 2012, *MNRAS*, **423**, 26
- Mattsson L., et al., 2014, *MNRAS*, **444**, 797
- Mayor M., Vigroux L., 1981, *A&A*, **98**, 1
- McKee C., 1989, in Allamandola L. J., Tielens A. G. G. M., eds, Vol. 135, *Interstellar Dust*, p. 431
- McKinnon R., Torrey P., Vogelsberger M., Hayward C. C., Marinacci F., 2017, *MNRAS*, **468**, 1505
- Melioli C., Brighenti F., D'Ercole A., de Gouveia Dal Pino E. M., 2009, *MNRAS*, **399**, 1089
- Miettinen O., et al., 2017, *A&A*, **606**, A17
- Morrissey P., et al., 2007, *ApJS*, **173**, 682
- Morselli L., et al., 2020, *MNRAS*, **496**, 4606
- Mott A., Spitoni E., Matteucci F., 2013, *MNRAS*, **435**, 2918
- Murante G., Monaco P., Borgani S., Tornatore L., Dolag K., Goz D., 2015, *MNRAS*, **447**, 178
- Naab T., Ostriker J. P., 2017, *ARA&A*, **55**, 59
- Nersesian A., et al., 2019, *A&A*, **624**, A80
- Noeske K. G., et al., 2007, *ApJ*, **660**, L47
- Oppenheimer B. D., Davé R., 2008, *MNRAS*, **387**, 577
- Pagel B. E. J., 1997, *Nucleosynthesis and Chemical Evolution of Galaxies*
- Palla M., Calura F., Matteucci F., Fan X. L., Vincenzo F., Lacchin E., 2020a, *MNRAS*, **494**, 2355
- Palla M., Matteucci F., Spitoni E., Vincenzo F., Grisoni V., 2020b, *MNRAS*, **498**, 1710
- Palla M., Santos-Peral P., Recio-Blanco A., Matteucci F., 2022, *A&A*, **663**, A125
- Pastrav B. A., 2020, *MNRAS*, **493**, 3580
- Perets H. B., Biham O., Manicó G., Pirronello V., Roser J., Swords S., Vidalí G., 2005, *ApJ*, **627**, 850
- Peters T., et al., 2017, *MNRAS*, **467**, 4322
- Pettini M., Pagel B. E. J., 2004, *MNRAS*, **348**, L59
- Pilbratt G. L., et al., 2010, *A&A*, **518**, L1
- Popescu C. C., Tuffs R. J., 2002, *MNRAS*, **335**, L41
- Popesso P., et al., 2019a, *MNRAS*, **483**, 3213
- Popesso P., et al., 2019b, *MNRAS*, **490**, 5285
- Popping G., Somerville R. S., Galametz M., 2017, *MNRAS*, **471**, 3152
- Portinari L., Chiosi C., 2000, *A&A*, **355**, 929
- Pozzi F., Calura F., Zamorani G., Delvecchio I., Gruppioni C., Santini P., 2020, *MNRAS*, **491**, 5073
- Priestley F. D., De Looze I., Barlow M. J., 2022, *MNRAS*, **509**, L6
- Putze A., Derome L., Maurin D., 2010, *A&A*, **516**, A66
- Reynolds C. S., Brenneman L. W., Lohfink A. M., Trippe M. L., Miller J. M., Fabian A. C., Nowak M. A., 2012, *ApJ*, **755**, 88
- Rimoldi A., Rossi E. M., Piran T., Portegies Zwart S., 2015, *MNRAS*, **447**, 3096
- Rockefeller G., Fryer C. L., Melia F., Warren M. S., 2004, *ApJ*, **604**, 662
- Rodighiero G., et al., 2010, *A&A*, **515**, A8
- Romano D., Matteucci F., Salucci P., Chiappini C., 2000, *ApJ*, **539**, 235
- Rupke D., 2018, *Galaxies*, **6**, 138
- Savage B. D., Sembach K. R., 1996, *ARA&A*, **34**, 279
- Scalo J. M., 1986, *Fundamentals Cosmic Phys.*, **11**, 1
- Schmidt M., 1959, *ApJ*, **129**, 243
- Schruba A., Leroy A. K., Walter F., Sandstrom K., Rosolowsky E., 2010, *ApJ*, **722**, 1699
- Silvia D. W., Smith B. D., Shull J. M., 2010, *ApJ*, **715**, 1575
- Smith D. J. B., Hayward C. C., 2018, *MNRAS*, **476**, 1705
- Somerville R. S., Davé R., 2015, *ARA&A*, **53**, 51
- Spitoni E., Matteucci F., 2011, *A&A*, **531**, A72
- Spitoni E., Romano D., Matteucci F., Ciotti L., 2015, *ApJ*, **802**, 129
- Spitoni E., Silva Aguirre V., Matteucci F., Calura F., Grisoni V., 2019, *A&A*, **623**, A60
- Spitoni E., Verma K., Silva Aguirre V., Calura F., 2020, *A&A*, **635**, A58
- Tacconi L. J., et al., 2010, *Nature*, **463**, 781
- Temim T., Dwek E., Tchernyshyov K., Boyer M. L., Meixner M., Gall C., Roman-Duval J., 2015, *ApJ*, **799**, 158
- Thon R., Meusinger H., 1998, *A&A*, **338**, 413
- Tinsley B. M., 1980, *Fundamentals Cosmic Phys.*, **5**, 287
- Toyouchi D., Chiba M., 2015, *ApJ*, **810**, 18
- Triani D. P., Sinha M., Croton D. J., Pacifici C., Dwek E., 2020, *MNRAS*, **493**, 2490
- Trčka A., et al., 2020, *MNRAS*, **494**, 2823
- Ural U., Wilkinson M. I., Read J. I., Walker M. G., 2015, *Nature Communications*, **6**, 7599
- Valiante R., Schneider R., Salvadori S., Bianchi S., 2011, *MNRAS*, **416**, 1916
- Viae S., et al., 2014, *A&A*, **567**, A71
- Vijayan A. P., Clay S. J., Thomas P. A., Yates R. M., Wilkins S. M., Henriques B. M., 2019, *MNRAS*, **489**, 4072
- Vincenzo F., Spitoni E., Calura F., Matteucci F., Silva Aguirre V., Miglio A., Cescutti G., 2019, *MNRAS*, **487**, L47
- Vogelsberger M., Marinacci F., Torrey P., Puchwein E., 2020, *Nature Reviews Physics*, **2**, 42

Walter F., Brinks E., de Blok W. J. G., Bigiel F., Kennicutt Robert C. J.,
 Thornley M. D., Leroy A., 2008, [AJ](#), **136**, 2563
 Werner M. W., et al., 2004, [ApJS](#), **154**, 1
 Yalinewich A., Piran T., Sari R., 2017, [ApJ](#), **838**, 12
 Yamasawa D., Habe A., Kozasa T., Nozawa T., Hirashita H., Umeda H.,
 Nomoto K., 2011, [ApJ](#), **735**, 44
 Zhang D., 2018, [Galaxies](#), **6**, 114
 da Cunha E., Charlot S., Elbaz D., 2008, [MNRAS](#), **388**, 1595
 de Vaucouleurs G., de Vaucouleurs A., Corwin Herold G. J., Buta R. J., Paturel
 G., Fouque P., 1991, Third Reference Catalogue of Bright Galaxies
 van den Hoek L. B., Groenewegen M. A. T., 1997, [A&AS](#), **123**, 305

This paper has been typeset from a \TeX/L\AA\TeX file prepared by the author.